 CMES, vol.55, no.3, pp.211-269, 2010

A 3D Frictionless Contact Domain Method for Large Deformation Problems

S. Hartmann[1], **R. Weyler**[2], **J. Oliver**[1]
J.C. Cante[2] **and J.A. Hernández**[1]

Abstract: This work describes a three-dimensional contact domain method for large deformation frictionless contact problems. Theoretical basis and numerical aspects of this specific contact method are given in [Oliver, Hartmann, Cante, Weyler and Hernández (2009)] and [Hartmann, Oliver, Weyler, Cante and Hernández (2009)] for two-dimensional, large deformation frictional contact problems. In this method, in contrast to many other contact formulations, the necessary contact constraints are formulated on a so-called contact domain, which can be interpreted as a fictive intermediate region connecting the potential contact surfaces of the deformable bodies. This contact domain has the same dimension as the contacting bodies. It will be endowed with a displacement field, interpolated from the displacements at the contact surfaces and will be subdivided into a non-overlapping set of contact patches, where the contact constraints will be applied. For the enforcement of these contact constraints a stabilized Lagrange multiplier method is used, which allows the condensation of the introduced Lagrange multipliers, leading to a purely displacement driven problem.

Keywords: Contact domain method, Interior penalty method, Stabilized Lagrange multipliers

1 Introduction

Although the numerical simulation of large deformation multibody contact problems is very important in numerous applications in many different fields of mechanical engineering, the solution of such contact problems still poses challenges in nonlinear structural mechanics. Consequently contact mechanics has deserved much

[1] E.T.S. d'Enginyers de Camins, Canals i Ports, Technical University of Catalonia (UPC), Campus Nord UPC, Mòdul C-1, c/Jordi Girona 1-3, 08034 Barcelona, Spain
[2] E.T.S. d'Enginyeries Industrial i Aeronàutica de Terrassa, Technical University of Catalonia (UPC), Campus Terrassa, c/Colom, 11, 08222 Terrassa, Spain

interest in many fields of computational modeling in engineering and sciences, see e.g. [Bardenhagen, Guilkey, Roessig, Brackbill, Witzel and Foster (2001); Vignjevic, De Vuyst and Campbell (2006); Willner (2009)]. A broad overview about the state-of-the-art on the mathematical basics as well as related computational techniques of contact mechanics is given for example in the monographs of Laursen (2002) and Wriggers (2006). The development of a computational contact strategy basically necessitates:

- A suitable method for the contact constraint enforcement
- A technique to discretize the contact surfaces.

As for the first point, various strategies for the variational enforcement of the contact constraints have been developed in the past, e.g. the penalty method, the Lagrange multiplier method or the augmented Lagrange method. All these methods have been applied together with specific collocation methods (e.g. [Heege and Alart (1996); Pietrzak and Curnier (1999); Simo and Laursen (1992)]) as well as with discretization methods based on a continuous treatment of the contact constraints (e.g. [Simo, Wriggers and Taylor (1985); Zavarise and Wriggers (1998)]). An overview of different constraint enforcement methods combined with varying discretization strategies can be found in Wriggers (1995). Yet another approach for the contact constraint enforcement, based on a formulation for the matching of different finite element meshes, introduced by Nitsche (1971), was used in recent publications [Heintz and Hansbo (2006); Wriggers and Zavarise (2008); Oliver, Hartmann, Cante, Weyler and Hernández (2009); Hartmann, Oliver, Weyler, Cante and Hernández (2009)]. The basic idea is to relate the Lagrange multiplier, representing the stresses in the contact interface, with the stress field of the contacting bodies at the contact boundary, in order to condense the introduced Lagrange multipliers. In this work, similar to [Oliver, Hartmann, Cante, Weyler and Hernández (2009); Hartmann, Oliver, Weyler, Cante and Hernández (2009)], the stabilized Lagrange multiplier method, initially presented in [Heintz and Hansbo (2006)], is generalized to the three-dimensional contact domain method for finite deformations.

As for the second point above, many of the contact algorithms developed in the past are based on a node-to-segment approach, developed by Hallquist, Goudreau and Benson (1985), which enforces the contact constraints at specific collocation points. Although this strategy is still widely used in many commercial finite element codes, some well-known drawbacks of this method need to be mentioned. In Papadopoulos and Taylor (1992) it has been shown that the satisfaction of the contact patch test cannot be guaranteed. Furthermore, the non-smooth discretization of the contact surfaces may lead to non-physical oscillations of the contact

forces in finite sliding problems, which has led to various developments of smoothing algorithms used together with node-to-segment formulations, see e.g. [Puso and Laursen (2002); Taylor and Wriggers (1999); Wriggers, Krstulovic-Opara and Korelc (2001)]. In recent years other discretization strategies were developed, based on a continuous treatment of the contact constraints. Most of these new segment-to-segment algorithms are based on the so-called mortar method, initially introduced in the context of domain decomposition methods [Bernardi, Debit and Maday (1990); Bernardi, Maday and Patera (1993); Bernardi, Maday and Patera (1994)]. The main idea of this method is the introduction of a weak, integral statement of the continuity constraint across the contact interface, instead of strong, pointwise constraints. On basis of the mortar method, numerous contact formulations have been developed in recent years. Algorithms using standard interpolations for the introduced Lagrange multipliers in the regime of small deformations, e.g. [Belgacem, Hild and Laborde (1998); McDevitt and Laursen (2000)] as well as its extension to finite deformation problems, e.g. [Puso and Laursen (2004a, 2004b); Yang, Laursen and Meng (2005); Fischer and Wriggers (2005); Fischer and Wriggers (2006); Puso, Laursen and Solberg (2008)] and mortar contact formulations based on so-called dual Lagrange multiplier spaces for small [Hüeber and Wohlmuth (2005); Hüeber, Stadler and Wohlmuth (2008)] and large deformations [Hartmann, Brunssen, Ramm and Wohlmuth (2007); Hartmann and Ramm (2008); Popp, Gee and Wall (2009)].

Nearly all of the proposed contact algorithms, no matter whether using a node-to-segment or a segment-to-segment contact discretization strategy, have in common that they project somehow one contact-surface/point (*slave/non-mortar*) onto the other contact-surface (*master/mortar*), in order to formulate the necessary contact conditions. Thus, the contact problem is defined on a subdomain, which is usually one dimension lower than the domain of the contacting bodies (see Fig. 1a). Recently, an alternative contact discretization strategy was developed in [Oliver, Hartmann, Cante, Weyler and Hernández (2009); Hartmann, Oliver, Weyler, Cante and Hernández (2009)], which uses a so-called contact domain to formulate the contact constraints. This contact domain has the same dimension as the contacting bodies and can be regarded as an intermediate region that connects the potential contact boundaries. The contact domain will be approximated with a set of non-overlapping patches, e.g. linear triangular patches for two-dimensional problems (see Fig. 1b) and [Oliver, Hartmann, Cante, Weyler and Hernández (2009); Hartmann, Oliver, Weyler, Cante and Hernández (2009)]) or linear tetrahedral patches in the three-dimensional regime (see section 3). Furthermore, the contact domain will be endowed with a displacement field, interpolated from the displacements of the boundaries of the contacting bodies. Consequently, the measurements of

the normal and tangential gaps as well as the introduced Lagrange multipliers are defined within the whole contact domain and not only along the contacting surfaces. This leads to a contact algorithm formulated in terms of a dimensionless, strain-like measure for the normal gap, based on the incremental motion of the contact domain. The necessary variation and linearization of the so-called normal gap intensity can be performed using standard manipulations of strain measures in classical continuum mechanics.

In their previous works [Oliver, Hartmann, Cante, Weyler and Hernández (2009)] and [Hartmann, Oliver, Weyler, Cante and Hernández (2009)], the authors have detailed in depth the theoretical basis of the so-called contact domain method as well as its finite element implementation for two-dimensional, large deformation frictional contact problems. These works have demonstrated that the contact-domain method displays a sound alternative in the field of computational contact mechanics, worth to be explored in more depth, particularly in a three-dimensional setup. Thus the present work describes the generalization, for the frictionless case, of the recently developed contact domain method to three-dimensional, finite deformation contact problems.

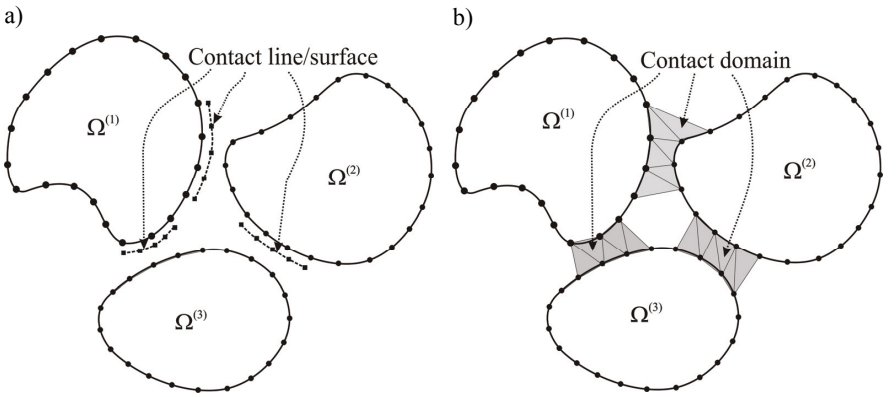

Figure 1: Imposition of contact constraints on the contacting bodies: a) Classical methods; b) contact domain method

The paper will be organized as follows: In section 2 a frictionless large deformation contact problem between two deformable bodies will be briefly described to introduce the notations used throughout this paper. Furthermore, some fundamental theoretical aspects of the contact domain method will be recalled together with the definition of the normal gap intensity. Section 2 closes with the presentation

of the stabilized variational formulation, as basis for the ensuing numerical implementation. The discretization of the contact domain with two different types of linear tetrahedral contact patches is detailed in section 3. It will be shown that the introduced Lagrange multipliers can be eliminated locally on patch level. Moreover the resulting contact contributions and their necessary linearization are derived. Finally a matrix notation for the contact residuals and the contact stiffness contributions are presented. The employed predictive active set strategy will be described in section 4, while the main focus of this part is on the description of some important additional technical aspects that come into play when moving from two to three dimensions. Some numerical examples will be analyzed in section 5 to demonstrate the performance of the proposed contact strategy. The paper closes with some concluding remarks in section 6.

2 Problem description

In this section a frictionless large deformation contact problem will be very briefly recalled to introduce some basic notations subsequently used in this paper. The already mentioned geometric contact domain will be specified together with its three-dimensional subdivision into linear tetrahedral contact patches. Furthermore, appropriate gap definitions for the contact domain method as well as the employed stabilized variational problem of the frictionless contact problem will be presented.

2.1 Basic notations

When considering contact problems, different contact scenarios like multiple contacts as well as self contact need to be faced. Without loss of generality, the subsequent description will be done on basis of one contact pair. A large deformation contact problem of two deformable bodies $\Omega^{(\alpha)}$, $\alpha = 1,2$, eventually coming into contact within a specific time step $[t_n, t_{n+1}]$ is shown in Fig. 2.

Therein

$$\mathbf{u}^{(\alpha)} = \mathbf{x}_{n+1}^{(\alpha)} - \mathbf{x}_n^{(\alpha)} \;\; \forall \mathbf{x}_n^{(\alpha)} \in \Omega_n^{(\alpha)} \tag{1}$$

defines the incremental displacement field of the two contacting bodies. The boundaries $\partial\Omega^{(\alpha)}$ of $\Omega^{(\alpha)}$ are divided into $\Gamma_u^{(\alpha)}$, where displacements are prescribed, $\Gamma_\sigma^{(\alpha)}$ where tractions are prescribed and a part $\Gamma_D^{(\alpha)}$ where the bodies might be in contact at the end of the time interval. It is assumed that the following conditions are satisfied:

$$\begin{aligned} &\Gamma_u^{(\alpha)} \cup \Gamma_\sigma^{(\alpha)} \cup \Gamma_D^{(\alpha)} = \partial\Omega^{(\alpha)} \text{ and} \\ &\Gamma_\sigma^{(\alpha)} \cap \Gamma_u^{(\alpha)} = \Gamma_\sigma^{(\alpha)} \cap \Gamma_D^{(\alpha)} = \Gamma_u^{(\alpha)} \cap \Gamma_D^{(\alpha)} = \emptyset. \end{aligned} \tag{2}$$

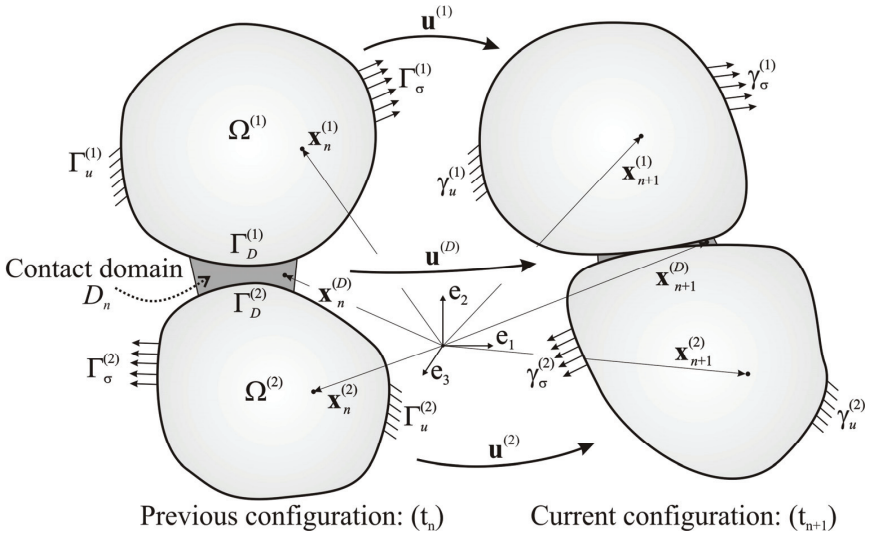

Figure 2: Two body large deformation contact problem in a specific time step $[t_n, t_{n+1}]$

2.2 Contact domain

Additionally a so-called *contact domain* D_n with boundary ∂D_n, joining part of the boundaries $\partial\Omega_n^{(\alpha)}$, i.e: $\Gamma_D^{(\alpha)} = \partial\Omega_n^{(\alpha)} \cap \partial D_n$, is defined (see Fig. 2). It has the same dimension as the contacting bodies and might be interpreted as a fictitious intermediate region connecting the potential contact surfaces of the deformable bodies. Assume that the boundaries $\Gamma_D^{(\alpha)}$ are large enough to contain those parts of $\partial\Omega_n^{(\alpha)}$ that are coming into contact at the end of the current time interval $[t_n, t_{n+1}]$ (thus at time t_{n+1}). Let $V_i^{(\alpha)}$ be a suitable number of vertices conveniently placed in the contacting boundaries $\Gamma_D^{(\alpha)}$. Based on these vertices, the contact domain D_n may be approximated by a domain D_n^l (where superscript l refers to the typical value of the vertices separation) partitioned in n_p patches $D_n^{(p)}$ such that

$$D_n \approx D_n^l = \bigcup_{p=1}^{n_p} D_n^{(p)}. \tag{3}$$

Remark 2.1. Although the vertices $V_i^{(\alpha)}$ might be, in principle, chosen independently of the discretization of the contacting bodies $\Omega^{(\alpha)}$, in the context of the finite element method the natural choice is that they coincide with the finite element

nodes on the contacting boundaries $\Gamma_D^{(\alpha)}$.

This partition of the contact domain has the following properties:

- It consists of a *unique layer of patches*.
- The contact patches $D_n^{(p)}$ *do not overlap*, and D_n^l converges to the contact domain D_n as the number of vertices increases (or, equivalently, $l \to 0$).

2.3 Approximation of the contact domain with contact patches

In this work, linear tetrahedral patches will be employed for the approximation of the introduced three-dimensional contact domain. Looking at Fig. 3 it is obvious that with this choice two different kinds of contact patches need to be distinguished. The so-called Type-A patches that have three vertex nodes placed on one contact boundary (defining the *base-face* of the corresponding tetrahedron) and one single node placed on the other, and the so-called Type-B patches that have two vertex nodes placed on either side of the contact surfaces (defining the two *base-lines*).

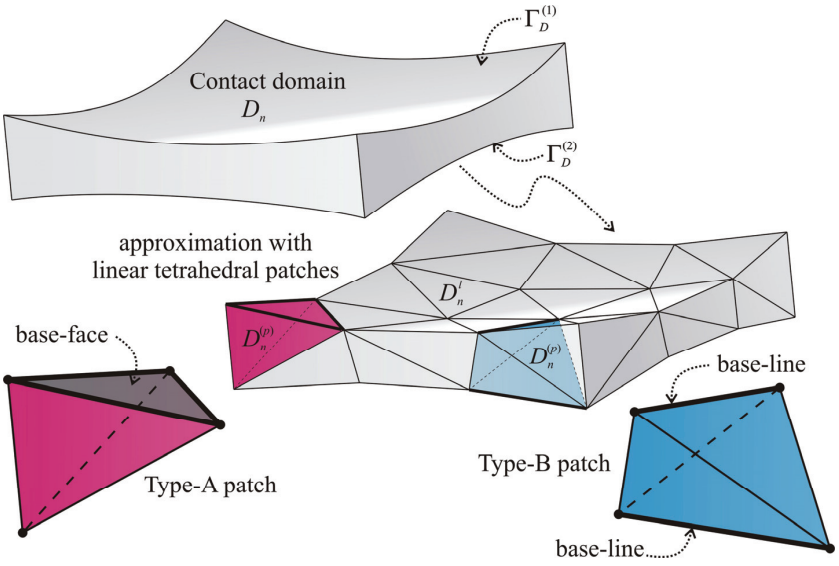

Figure 3: 3D contact domain and its approximation with linear tetrahedral patches

2.3.1 Construction of the contact domain tetrahedralization

The construction of the aforementioned approximation of the contact domain with linear tetrahedral contact patches can be viewed as a kind of contact searching algorithm that pairs possible contact boundaries. In this work, a general strategy is presented, which can naturally be applied to any contact scenario, including self-contact as well as contact between multiple deformable bodies. It is based on a so-called constraint Delaunay tesselation, which will be explained in the following.

In Fig. 4 the basic steps of the approximation of the contact domain are shown exemplarily for a two-dimensional setting. Two discretized bodies, eventually being in contact, are depicted in Fig. 4a. As the contact domain to be approximated should have the properties to connect the boundary nodes of the discretized bodies, a first step is to remove all the interior finite element nodes, such that the remaining nodes only define the boundaries of the discretized bodies. A key step in the generation process is the so-called *shrinkage* of the bodies. The outward normals of the boundary nodes are computed as the weighted average of the normals of the adjacent boundary faces. Then the boundary nodes are offset in the negative direction of its outward normal by a user defined distance (shrinkage parameter), depending upon the element size. The removal of the interior nodes as well as the offset of the boundary nodes is shown exemplarily for a two-dimensional setting in Fig. 4b. An appropriate shrinkage of the boundary is necessary to guarantee that the potential contact boundaries are separated from each other, in such a way that an automatic mesh generation algorithm can generate a tetrahedralization of the space (gap) between the displaced boundary nodes. Having repositioned the boundary nodes of the contacting bodies, the triangulation of the discretized boundary is passed together with the outward normals to an automatic mesh generation algorithm, which connects the boundary nodes under the following constraints:

- The generated interface mesh should be composed solely of finite element nodes at the contacting boundaries, without introducing interior vertices (single layer contact domain).
- The faces of the constructed interface mesh should match the faces of the finite elements at the contact boundary.

Another parameter (the alpha shape parameter [Idelsohn, Onate, Calvo and Del Pin (2003)]) will be supplied to the mesher in order to only connect boundary nodes that are sufficiently close to each other. Thus the resulting contact domain mesh only connects finite element nodes at the boundary that may be potential vertices to come into contact in the subsequent time step. The result of this automatic mesh generation is shown for a two-dimensional case in Fig. 4c. It is worth noting that,

for the implementation of the presented contact strategy, *only the connectivity* of the constructed contact patches will be needed and it *will be worked with the original spatial position of the finite element nodes placed at the boundaries* of the contacting bodies (see Fig. 4d). Therefore, the repositioning of the boundary nodes (shrinkage) is only a technical necessity to guarantee that the automatic meshing algorithm is able to build up the connectivity of the resulting contact domain patches, and does not introduce any form of modification of the geometrical description of the discretized contacting bodies.

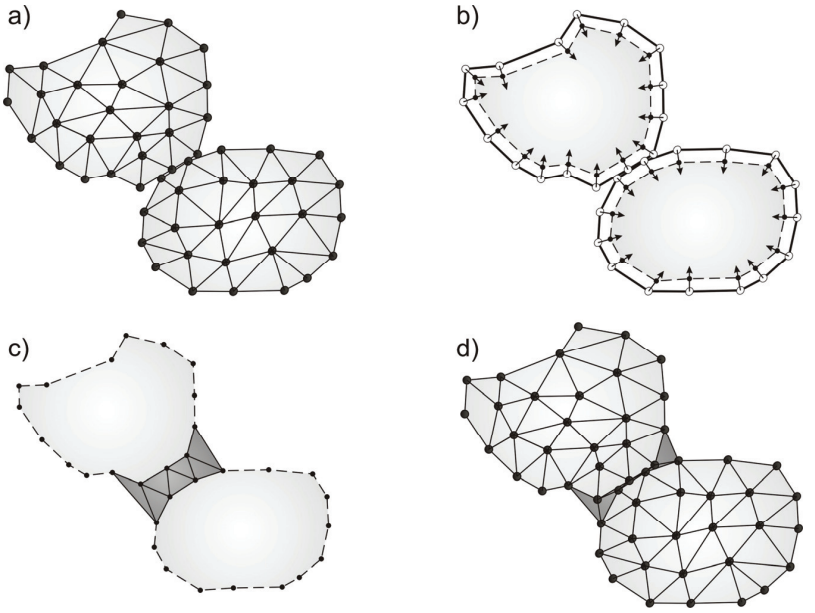

Figure 4: Generating the contact domain mesh in a two-dimensional setting: a) two meshed bodies; b) removal of the interior nodes and shrinkage of the boundary; c) construction of the contact domain mesh; d) retrieve of the original boundary and mesh

2.4 Incremental motion

Regardless of the type of contact patch, yet another incremental displacement field $\mathbf{u}^{(D)}$ is defined within the contact domain patches $D_n^{(p)}$, which describes the motion of any point within this domain, during the current time step. It is linearly interpolated from the corresponding incremental displacements at the contacting

boundaries and can be specified by

$$\mathbf{u}^{(D)}(\mathbf{x}_n) \equiv \mathbf{u}^{(p)}(\mathbf{x}_n) = \sum_{i=1}^{4} N_i(\mathbf{x}_n)\,\mathbf{d}_i^{(D)} \quad \forall \mathbf{x}_n \in D_n^{(p)} \tag{4}$$

when using linear tetrahedral patches. Herein N_i are the standard linear interpolation functions for linear tetrahedral finite elements [Zienkiewicz and Taylor (2000)] and $\mathbf{d}_i^{(D)}$ are *the incremental displacements* at the vertices $1,2,3,4$ of a contact patch p. Due to the linear format of the incremental displacement in Eq.4, the convected contact domain D_{n+1}^{l} is also a linear tetrahedralization, approximating the current contact domain D_{n+1}. One can now define strain measures of this motion, in particular the *incremental gradient of deformation tensor*:

$$\mathbf{f}^{(D)} = \frac{\partial \mathbf{x}_{n+1}}{\partial \mathbf{x}_n} = \mathbf{1} + GRAD\left(\mathbf{u}^{(D)}\right) \tag{5}$$

where $\mathbf{1}$ stands for the second order unit tensor.

Remark 2.2. Notice that, due to the linear character of the incremental displacement field in Eq.4, $GRAD\left(\mathbf{u}^{(D)}\right)$ and $\mathbf{f}^{(D)}$ are *constant within every contact patch*, i.e.:

$$\mathbf{f}^{(D)}(\mathbf{x}_n) \equiv \mathbf{f}^{(p)} = \text{constant} \;\; \forall \mathbf{x}_n \in D^{(p)} \tag{6}$$

2.5 Geometrical normal gap

A specific feature of working with a contact domain method is the fact that the utilized gaps are defined for every point within the contact domain. Facing a frictionless contact scenario, only the normal gap needs to be specified. Starting from the previous configuration and considering, in a first stage, a Type-A patch, the *initial normal gap* G_N will be defined for every given point of the contact patch $\mathbf{x}_n \in D_n^{(p)}$ (at the previous configuration) as the signed distance from its N-projection (according to the normal $\mathbf{N}$) on the base-face $\bar{\mathbf{x}}_n \in \Gamma_D^{(\alpha)}$ (see Fig. 5), i.e.:

$$G_N(\mathbf{x}_n) = (\mathbf{x}_n - \bar{\mathbf{x}}_n) \cdot \mathbf{N}(\mathbf{x}_n) \tag{7}$$

In the current contact patch $D_{n+1}^{(p)}$, the *final gap vector* $\mathbf{g}(\mathbf{x}_n)$(at the current configuration) is defined with

$$\mathbf{g}(\mathbf{x}_n) = \mathbf{x}_{n+1} - \bar{\mathbf{x}}_{n+1} \tag{8}$$

where $\mathbf{x}_{n+1}$ and $\bar{\mathbf{x}}_{n+1}$ are the convected points of $\mathbf{x}_n$ and $\bar{\mathbf{x}}_n$, respectively. The definition for the normal gap g_N is then given as the projections of the final gap vector $\mathbf{g}(\mathbf{x}_n)$ onto the current normal direction.

$$g_N(\mathbf{x}_n) = \mathbf{g}(\mathbf{x}_n) \cdot \mathbf{n}^{(p)} \tag{9}$$

Herein $\mathbf{n}^{(p)}$ stands for the normal to the base-face of the convected patch $D^{(p)}_{n+1}$.

Remark 2.3. Notice that the definition of the normal gap in Eq.9 i*s completely equivalent to the (signed) distance* from a point $\mathbf{x}_{n+1}$ to the base-face of the corresponding contact patch $D^{(p)}_{n+1}$. Thus, negative values of g_N indicate penetration of the considered point.

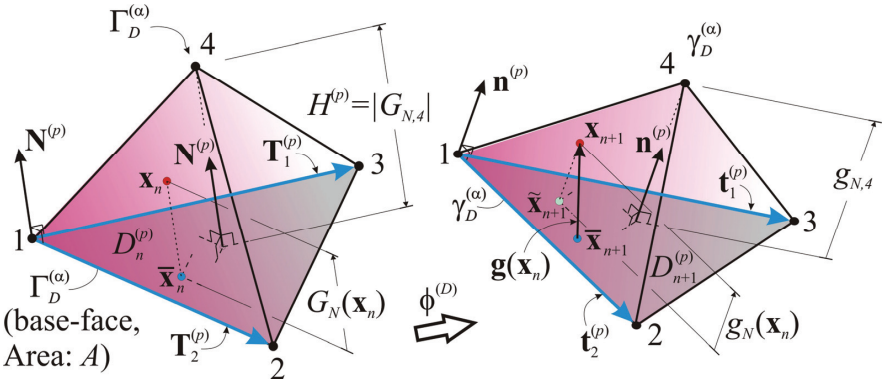

Figure 5: Linear tetrahedral contact patch (Type-A) in previous and current configuration

Due to the linear incremental displacement field within one contact patch in Eq.4 and the resulting constant character of $\mathbf{f}^{(p)}$ in Eq.6, the final gap vector $\mathbf{g}(\mathbf{x}_n)$ can be written as

$$\mathbf{g}(\mathbf{x}_n) = \mathbf{x}_{n+1} - \bar{\mathbf{x}}_{n+1} = G_N(\mathbf{x}_n)\,\mathbf{f}^{(p)} \cdot \mathbf{N}^{(p)} \tag{10}$$

which leads to the expression for the normal gap in Eq.9:

$$g_N(\mathbf{x}_n) = \mathbf{n}^{(p)} \cdot \mathbf{g}(\mathbf{x}_n) = G_N(\mathbf{x}_n)\,\mathbf{n}^{(p)} \cdot \mathbf{f}^{(p)} \cdot \mathbf{N}^{(p)} \tag{11}$$

Remark 2.4. After some algebraic manipulation, it can be proven that the mathematical expression of the normal gap in Eq.11 coincides with the one in a classical

node-to-surface formulation using a three-node master segment [Wriggers (2006)] if $\mathbf{x}_n$ is considered *the (slave) node*, and the base-face of the tetrahedra is considered *the (master) segment*. However, there are some remarkable differences emerging from Eq.11:

- The normal gap is here defined for *all points of the contact patch* $D_n^{(p)}$ and not only for the vertices (nodes) in the contacting boundaries $\Gamma_D^{(\alpha)}$. This is going to be exploited for the mathematical and numerical formulation of the contact problem.
- The normal gap is defined in *terms of strain measures* $(\mathbf{f}^{(p)}, GRAD(\mathbf{u}^{(p)}))$ of the incremental displacement motion endowed to the contact domain. This allows the straightforward generalization to tetrahedral contact patches of any shape and, more specifically, to contact patches having two vertices on either side of the contacting boundaries (Type-B patch), which will be shown later in this paper.

2.6 Normal gap intensity

As mentioned above, a distinguishing feature of the proposed method is the usage of dimensionless, strain-like measures to formulate the geometrical contact constraints. Therefore, from Eq.11, the so-called normal gap intensity

$$\bar{g}_N^{(p)} = \frac{g_N(\mathbf{x}_n)}{|G_N(\mathbf{x}_n)|} = sign\left(G_N(\mathbf{x}_n)\right) \mathbf{n}^{(p)} \cdot \mathbf{f}^{(p)} \cdot \mathbf{N}^{(p)} \tag{12}$$

is defined by dividing the geometrical gap with the absolute value of the initial normal gap. Although the geometrical normal gap $g_N(\mathbf{x}_n)$, which is defined for every point $\mathbf{x}_n$ within the contact domain through Eq.11, may vary within a specific contact patch, it needs to be emphasized that the corresponding normal gap intensity turns out to be patch-wise constant. Therefore the superscript $(\bullet)^{(p)}$ in Eq.12 identifies the patch-wise constant entities.

Remark 2.5. In view of Eq.12 one may wonder about the singularity of the normal gap intensity $\bar{g}_N$ when $G_N(\mathbf{x}_n) = 0 \ \forall \mathbf{x}_n \in D_n^{(p)}$ (perfect normal contact in the patch at the previous configuration). Then, $\bar{g}_N$ could become unbounded, this possibly translating into ill conditioning of the formulation. However, it was demonstrated in the previous works [Oliver, Hartmann, Cante, Weyler and Hernández (2009); Hartmann, Oliver, Weyler, Cante and Hernández (2009)] that the introduced normal gap intensity $\bar{g}_N$ only appears in integral expressions of the type

$$\int_{D_n^{(p)}} (\bullet) \bar{g}_N(\mathbf{x}_n) \, dD \tag{13}$$

This type of integral will converge to bounded values and, thus, the unbounded character of the gap intensity $\bar{g}_N$ does not translate into ill conditioning of the problem (see also Remark 3.2).

2.7 Normal contact constraints

In a frictionless contact problem only the normal contact constraints need to be considered. Let $\mathbf{P}^{(\alpha)}(\mathbf{x}_n, t_{n+1})$ denote the first Piola-Kirchhoff stresses, at the current time t_{n+1}, measured with respect to the previous ($\Omega_n^{(\alpha)}$) configuration and

$$\mathbf{t}_c(\mathbf{x}_n, \mathbf{N}) = \mathbf{P}^{(\alpha)} \cdot \mathbf{N} \quad \forall \mathbf{x}_n \in \Gamma_D^{(\alpha)} \tag{14}$$

the traction vector acting onto the N-oriented contact surface, where the normal $\mathbf{N}$ is patch-wise defined in the previous contact domain D_n^l (see sections 3.1.1 and 3.2.1). Assuming that adhesion is excluded in the contact area, the normal contact traction

$$t_N^{(\alpha)}(\mathbf{x}_n) = \mathbf{n} \cdot \mathbf{t}_c = \mathbf{n} \cdot \mathbf{P}^{(\alpha)} \cdot \mathbf{N} \quad \forall \mathbf{x}_n \in \Gamma_D^{(\alpha)} \tag{15}$$

must be negative ($t_N^{(\alpha)} \leq 0$). In Eq.15 $\mathbf{n}$ is the patch-wise defined normal in the current contact domain D_{n+1}^l. Additionally the geometrical *impenetrability constraint*

$$\bar{g}_N(\mathbf{x}_n) \geq 0 \quad \forall \mathbf{x}_n \in D_n^l \tag{16}$$

must be satisfied in the contact domain D_n^l. As the normal contact traction $t_N^{(\alpha)}$ only lives on the contacting boundaries $\Gamma_D^{(\alpha)}$, *a normal Lagrange multiplier* $\lambda_N(\mathbf{x}_n)$ $\forall \mathbf{x}_n \in D_n^l$ is introduced, *living in the whole previous contact domain* and fulfilling

$$\begin{cases} \lambda_N \equiv \lambda_N(\mathbf{x}_n) & \forall \mathbf{x}_n \in D_n^l \\ \lambda_N(\mathbf{x}_n) = t_N^{(\alpha)}(\mathbf{x}_n) & \forall \mathbf{x}_n \in \Gamma_D^{(\alpha)} \end{cases} \tag{17}$$

Therefore, the normal contact constraints may be summarized in form of the classical *Karush-Kuhn-Tucker* conditions [Wriggers (2006)], using the introduced normal Lagrange multiplier

$$\lambda_N \leq 0, \; \bar{g}_N \geq 0, \; \lambda_N \bar{g}_N = 0 \text{ in } D_n^l \tag{18}$$

2.8 Boundary value problem

2.8.1 Inequality constrained problem

As the geometrical definitions, introduced so far, are based on the incremental displacements $\mathbf{u}^{(\alpha)}(\mathbf{x}_n^{(\alpha)})$ in Eq.1, the inequality constrained boundary value problem

will be written in a consistent way, taking those displacements as primal unknowns, i.e.:

$$FIND: \begin{cases} \mathbf{u}^{(\alpha)}(\mathbf{x}_n): & \Omega_n^{(\alpha)} \rightarrow \mathrm{R}^3 \\ \lambda_N(\mathbf{x}_n): & D_n \rightarrow \mathrm{R} \end{cases} \tag{19}$$

$FULFILLING:$

Momentum Equation

$$\rho^{(\alpha)}\ddot{\mathbf{u}}^{(\alpha)} = DIV\mathbf{P}^{(\alpha)} + \mathbf{b}^{(\alpha)} \text{ in } \Omega_n^{(\alpha)} \tag{20}$$

Constitutive Model

$$\mathbf{P}^{(\alpha)} = \Sigma^{(\alpha)}\left(\mathbf{u}^{(\alpha)}\right) \text{ in } \Omega_n^{(\alpha)} \tag{21}$$

Dirichlet's boundary conditions

$$\mathbf{u}^{(\alpha)} = \hat{\mathbf{u}}^{(\alpha)} \text{ in } \Gamma_u^{(\alpha)} \tag{22}$$

Neumann's boundary conditions

$$\mathbf{P}^{(\alpha)} \cdot \boldsymbol{\nu}^{(\alpha)} = \hat{\mathbf{t}}^{(\alpha)} \text{ in } \Gamma_\sigma^{(\alpha)} \tag{23}$$

Lagrange multiplier identification

$$\lambda_N = t_N^{(\alpha)} \text{ in } \Gamma_D^{(\alpha)} \tag{24}$$

Normal contact constraints

$$\lambda_N \leq 0,\ \bar{g}_N\left(\mathbf{u}^{(D)}\right) \geq 0,\ \lambda_N \bar{g}_N\left(\mathbf{u}^{(D)}\right) = 0 \text{ in } D_n \tag{25}$$

Herein $\mathbf{P}^{(\alpha)}$ and $\mathbf{b}^{(\alpha)}$ are the first Piola-Kirchhoff stress tensor (measured at the previous configuration $\Omega_n^{(\alpha)}$ and given via an appropriate constitutive relation in Eq.21), and the body forces on $\Omega^{(\alpha)}$, respectively. Furthermore, $\ddot{\mathbf{u}}^{(\alpha)}$ and $\rho^{(\alpha)}$ represent the material acceleration field and the density of the bodies, respectively. The appropriate boundary conditions are given by the prescribed displacements $\hat{\mathbf{u}}^{(\alpha)}$ and tractions $\hat{\mathbf{t}}^{(\alpha)}$, acting on the correlated boundaries $\Gamma_u^{(\alpha)}$ and $\Gamma_\sigma^{(\alpha)}$. The gap expression $\bar{g}_N(\mathbf{u}^{(D)})$ in Eq.25 is the one in Eq.12. Then, the incremental displacements at the contact domain $\mathbf{u}^{(D)} \equiv \mathbf{u}^{(p)}$ are explicitly defined via Eq.4, in terms of the incremental displacements at the vertices of the triangulation, $\mathbf{d}_i^{(D)}(\mathbf{u}^{(\alpha)})$, which, in turn, are implicitly defined in terms of the primal unknowns $\mathbf{u}^{(\alpha)}(\mathbf{x}_n)$.

Remark 2.6. The boundary value problem (BVP) given in Eqs.19-25 is written in an *incremental manner*, which means that the *previous* configuration is taken to be the reference configuration. For example the first Piola-Kirchhoff stress tensor $\mathbf{P}^{(\alpha)}$ is not based on the initial, undeformed configuration but on the *previous* one. However, one could have written the motion for the deformable bodies in the classical total *Lagrangean manner* as well (taking the initial configuration as the reference one) and *restrict the incremental setting to the contact part of the problem*. Nevertheless and only for the sake of clearness and simplicity in the explanation, the authors have decided to write the whole boundary value problem in that incremental manner. In other words: The method does not place any limitation on the selected description of the contacting bodies motion.

2.8.2 Equality constrained problem

In the context of large deformation contact problems the size and position of the contact interfaces may change permanently. Therefore an active set strategy is utilized to identify the present contact area on basis of the normal Karush-Kuhn-Tucker conditions given in Eqs.18. It will be assumed that the active normal contact domain $D_n^{(N)}$ *is known in advance* as a result of the active set strategy, described in detail in [Oliver, Hartmann, Cante, Weyler and Hernández (2009); Hartmann, Oliver, Weyler, Cante and Hernández (2009)] which is based on the following criteria:

$$D_n^{(N)} := \{\mathbf{x}_n \mid \lambda_N(\mathbf{x}_n) < 0\} \tag{26}$$

which, in view of the equality $\lambda_N \bar{g}_N = 0$ in Eq.18, implies:

$$\bar{g}_N(\mathbf{x}_n) = 0 \;\; \forall \mathbf{x}_n \in D_n^{(N)} \tag{27}$$

Then, in view of Eq.18, the definition for the active normal contact domain in Eq.26 and Eq.27 provide the following trivial solution for the normal Lagrange multiplier λ_N in the complementary domain $D_n \backslash D_n^{(N)}$:

$$\begin{cases} \lambda_N(\mathbf{x}_n) \leq 0 & \forall \mathbf{x}_n \in D_n \\ \lambda_N(\mathbf{x}_n) < 0 & \forall \mathbf{x}_n \in D_n^{(N)} \end{cases} \Rightarrow \lambda_N(\mathbf{x}_n) = 0 \;\; \forall \mathbf{x}_n \in D_n \backslash D_n^{(N)} \tag{28}$$

Therefore, the complementary domain $D_n \backslash D_n^{(N)}$ *can be excluded* from the boundary value problem, which now reads:

$$FIND: \begin{cases} \mathbf{u}^{(\alpha)}(\mathbf{x}_n): & \Omega_n^{(\alpha)} \rightarrow \mathrm{R}^3 \\ \lambda_N(\mathbf{x}_n): & D_n^{(N)} \rightarrow \mathrm{R}^- \end{cases} \tag{29}$$

Additionally, Eq.25 of *the inequality constrained problem* now changes to Constraint condition

$$\bar{g}_N = 0 \text{ in } D^{(N)} \tag{30}$$

where now Eq.30 *is an equality constraint* in terms of the normal gap intensitiy $\bar{g}_N$.

2.9 Variational problem

For applying a finite element discretization scheme to solve contact problems, an appropriate weak form of the underlying equality constrained boundary value problem given in section 2.8.2 is needed. The *contact domain method* presented in [Oliver, Hartmann, Cante, Weyler and Hernández (2009)] and [Hartmann, Oliver, Weyler, Cante and Hernández (2009)] enforces the contact constraints using a generalization of the stabilized Lagrange multiplier method employed in [Heintz and Hansbo (2006)]. In addition, the method is exploited for the condensation of the introduced normal Lagrange multiplier (λ_N), which represents the normal contact tractions at the contacting boundaries. A detailed theoretical basis for the employed variational equations can be found in [Oliver, Hartmann, Cante, Weyler and Hernández (2009)]. Using appropriate spaces for the incremental displacements $\mathbf{u} = \left[\mathbf{u}^{(\alpha)}, \mathbf{u}^{(D)}\right]$, and their variations $\delta\mathbf{u} = \left[\delta\mathbf{u}^{(\alpha)}, \delta\mathbf{u}^{(D)}\right]$ (virtual displacements), as well as for the introduced normal Lagrange multiplier λ_N and their variations $\delta\lambda_N$, the employed variational equations can be summarized as follows:

The virtual work principle reads

$$\delta\Pi_{mech}(\mathbf{u}, \lambda_N, \delta\mathbf{u}) := \delta\Pi_{int,ext}(\mathbf{u}^{(\alpha)}, \delta\mathbf{u}^{(\alpha)}) + \delta\Pi_{cont}(\mathbf{u}^{(D)}, \delta\mathbf{u}^{(D)}, \lambda_N) = 0 \quad \forall\delta\mathbf{u} \tag{31}$$

where $\delta\Pi_{mech}$ is the total virtual mechanical work and $\delta\Pi_{int,ext}$ denotes the sum of the virtual work arising from the internal and external forces of the contacting bodies. Various variational energy principles can be used to derive an expression for the virtual work done by the internal and external forces of the respective body. As the present work concentrates on the description of the contact phenomena, the main focus of this work will be on the second contribution in Eq.31, namely the contact virtual work $\delta\Pi_{cont}$. Using the variations of the normal gap intensity, the contact virtual work expression can be written as

$$\delta\Pi_{cont}\left(\mathbf{u}^{(D)}, \delta\mathbf{u}^{(D)}, \lambda_N\right) = \int_{D_n^{(N)}} \lambda_N \delta\bar{g}_N \, dD. \tag{32}$$

For the enforcement of the normal contact constraints, an additional variational

equation

$$\delta\Pi_{\lambda_N}(\mathbf{u},\lambda_N,\delta\lambda_N)=\int_{D^{(N)}}\delta\lambda_N\bar{g}_N dD+\underbrace{\int_{\partial D_n^{(N)}\cap\Gamma_D^{(\alpha)}}\delta\lambda_N\tau(t_N-\lambda_N)\,d\Gamma}_{\text{additional term}}=0\quad\forall\delta\lambda_N \tag{33}$$

is derived. Eq.33 is the (stabilized) variational constraint equation to enforce the normal contact conditions within the appropriate active normal contact domain $D_n^{(N)}$. The additional term in Eq.33 can be interpreted as a stabilization term, which allows the condensation of the introduced normal Lagrange multiplier, where τ is a user defined stabilization parameter, which will be discussed later. Furthermore, t_N is the projection of the traction vector at the boundaries of the contacting bodies onto the current normal direction, given in Eq.15.

3 Discretization of the contact domain

To solve the variational problem in Eq.31, the deformable bodies $\Omega^{(\alpha)}$ as well as the contact domain D_n are discretized using finite elements and contact patches. The discretization of the contacting bodies is done using standard, linear tetrahedral finite elements. This allows an easy evaluation of the discrete variational constraint equations, as the stress field within such an element is constant (see sections 3.1.2 and 3.2.2).

Working with the stabilized variational Eq.31 and Eq.33, suitable approximations for the introduced normal Lagrange multiplier have to be chosen. In this work, a *patch-wise constant approximation*

$$\lambda_N\approx\lambda_N^h=\sum_{p=1}^{n_N}\psi^{(p)}\Lambda_N^{(p)}\text{ with }\psi^{(p)}(\mathbf{x}_n)=\begin{cases}1 & \forall\mathbf{x}_n\in D_n^{(p)}\\ 0 & \forall\mathbf{x}_n\notin D_n^{(p)}\end{cases} \tag{34}$$

is used, where n_N indicates the number of patches of the active normal contact domain. Furthermore, $\Lambda_N^{(p)}$ represents the discrete (constant) value of the normal Lagrange multiplier in a specific contact patch. All the subsequent explanations in this section are based on one contact domain patch, therefore the super-/subscripts $(\bullet)_n^{(p)}$ will be omitted in the following.

As already introduced in the previous section, the subdivision of the contact domain will be done using linear, tetrahedral contact patches, where two different types (A and B) have to be distinguished. Their specific differences and handling within the contact algorithm will be detailed in the following.

3.1 Type-A contact patch

A typical contact patch of Type-A is shown in Fig. 5 in both the previous and the current configuration. It is characterized by the fact that three vertex nodes (1,2,3) are placed on the boundary of one contacting body, and that the remaining node 4 is placed on the boundary of the other body.

3.1.1 Geometrical properties

Geometrical properties in the *previous* configuration are defined and calculated with:
Covariant tangent vectors

$$\mathbf{T}_1 = \mathbf{x}_{n,2} - \mathbf{x}_{n,1} \text{ and } \mathbf{T}_2 = \mathbf{x}_{n,3} - \mathbf{x}_{n,1}. \tag{35}$$

Remark 3.1. Note that, throughout this paper, the notations $(\bullet)_{\bullet,I}$ or $(\bullet)_{\bullet,IJ}$ are been used to identify entities that are connected to the specified vertex nodes I or J and will not indicate a partial derivative with respect to any direction.

Unit normal vector

$$\mathbf{N} = \frac{\mathbf{T}_1 \times \mathbf{T}_2}{\|\mathbf{T}_1 \times \mathbf{T}_2\|} \tag{36}$$

The *initial normal gap* of the single vertex node 4 (sign-sensitive)

$$G_{N,4} = (\mathbf{x}_{n,4} - \mathbf{x}_{n,1}) \cdot \mathbf{N} \tag{37}$$

The *initial height* of the contact patch, which is equivalent with the absolute value of the initial normal gap vertex node 4

$$H = |G_{N,4}|. \tag{38}$$

The *area* of the base triangle (base-face) is given by

$$A = \frac{1}{2} \|(\mathbf{x}_{n,2} - \mathbf{x}_{n,1}) \times (\mathbf{x}_{n,3} - \mathbf{x}_{n,1})\| = \frac{1}{2} \|\mathbf{T}_1 \times \mathbf{T}_2\| \tag{39}$$

And the *volume* of the Type-A contact patch is

$$V = \frac{1}{3} AH \tag{40}$$

3.1.2 Local constraint enforcement

Due to the piece-wise constant approximation of the introduced normal Lagrange multiplier and the patch-wise constant character of the normal gap intensity, the discretized version of the stabilized, variational constraint Eq.33

$$\delta\Pi^h_{\lambda_N}(\mathbf{d},\Lambda_N,\delta\Lambda_N)=\int_D \delta\Lambda_N\bar{g}_N dD+\int_\Gamma \delta\Lambda_N\tau\,(t_N-\Lambda_N)\,d\Gamma=0 \tag{41}$$

can be decoupled and thus enforced separately for every single contact domain patch. Herein Γ stands for the surface of the base-face of the contact patch tetrahedron and t_N is the normal traction in that finite element of the contacting body sharing the common face (base-face) with the contact domain patch (see Eq.15 and Fig. 6). As the spatial discretization of the contacting bodies is done with linear tetrahedral finite elements, the stress field in the solids is constant within one finite element and therefore the tractions are constant along the common face. Employing a patch-wise constant stabilization parameter τ, the integration of the discrete variational constraint Eq.41 can be done analytically using

$$\int_D dD=V=\frac{1}{3}AH \text{ and } \int_\Gamma d\Gamma=A \tag{42}$$

Inserting Eq.42 into Eq.41 yields

$$\frac{1}{3}AH\bar{g}_N+A\tau\,(t_N-\Lambda_N)=0 \quad\Rightarrow\quad \frac{1}{3}H\bar{g}_N+\tau t_N=\tau\Lambda_N\,, \tag{43}$$

which can be directly solved for the discrete normal Lagrange multiplier as:

$$\Lambda_N=t_N+\frac{H}{3\tau}\bar{g}_N \tag{44}$$

In section 2.6, the patch-wise constant normal gap intensity $\bar{g}_N$ was introduced and defined in Eq.12. Alternatively, this *constant* normal gap intensity can be expressed using the current geometrical normal gap of the vertex node 4

$$g_{N,4}=(\mathbf{x}_{n+1,4}-\mathbf{x}_{n+1,1})\cdot\mathbf{n} \tag{45}$$

divided by the elemental height (Eq.38)

$$\bar{g}_N=\frac{g_N(\mathbf{x}_n)}{|G_N(\mathbf{x}_n)|}=\frac{g_{N,4}}{|G_{N,4}|}=\frac{g_{N,4}}{H} \tag{46}$$

Using Eq.46, the evaluation of the normal Lagrange multiplier in Eq.44 can be simplified to

$$\Lambda_N=t_N+\frac{1}{3\tau}g_{N,4} \tag{47}$$

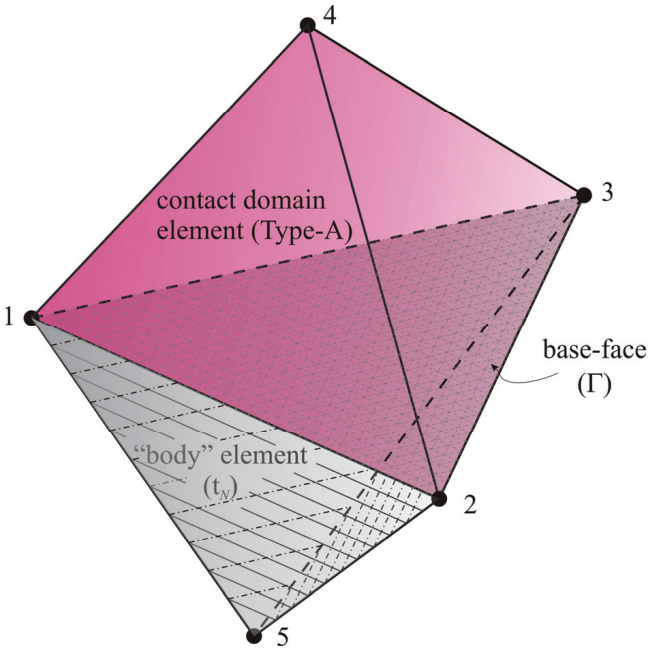

Figure 6: Contact domain patch (Type-A) with adjacent "body" element

3.2 Type-B contact patch

A typical contact patch of Type-B is shown in Fig. 7 in both the previous and the current configuration. It is characterized by the fact that two vertex nodes (1,2 and 3,4) are placed on either boundary of the two contacting bodies, respectively.

3.2.1 Geometrical properties

Geometrical properties in the *previous* configuration are defined and calculated with:
Using the definition of the covariant tangent vectors

$$\mathbf{T}_1 = \mathbf{x}_{n,2} - \mathbf{x}_{n,1} \text{ and } \mathbf{T}_2 = \mathbf{x}_{n,3} - \mathbf{x}_{n,4} \tag{48}$$

the unit normal vector, the initial (elemental) normal gap and the initial (elemental) height are computed in the same manner as for Type-A patches, using Eqs.36-38, but replacing $G_{N,4}$ with $G_{N,34}$. Furthermore the volume of the element

$$V = \frac{1}{6} \|\mathbf{T}_1 \times \mathbf{T}_2\| H = \frac{1}{3} A^* H \tag{49}$$

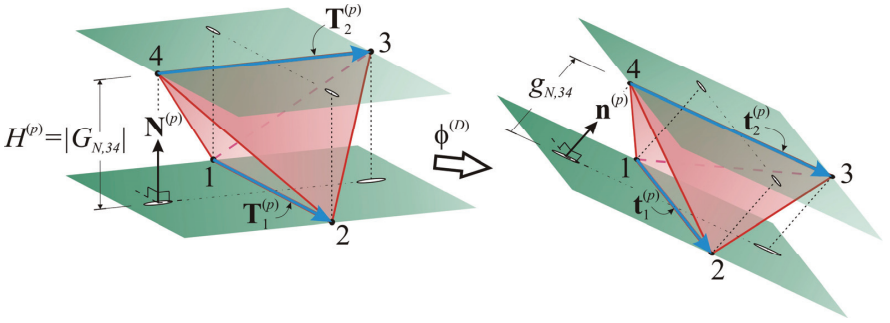

Figure 7: Linear tetrahedral contact patch (Type-B) in previous and current configuration

is computed using the definition of an artificial area

$$A^* = \frac{1}{2}\|\mathbf{T}_1 \times \mathbf{T}_2\| \tag{50}$$

Finally the *lengths* of the base-edges are defined with

$$L_1 = \|\mathbf{x}_{n,2} - \mathbf{x}_{n,1}\| \text{ and } L_2 = \|\mathbf{x}_{n,3} - \mathbf{x}_{n,4}\|. \tag{51}$$

3.2.2 *Local constraint enforcement*

In section 3.1, it was shown that the variational constraint Eq.33 can be decoupled and integrated analytically for Type-A patches. In case of Type-B patches, it is a little more complicated, as a contact domain patch now might share a common edge with various finite elements in the contacting body (see Fig. 8).

The adjacent "body" elements are needed to compute the normal traction (t_N) for the additional stabilization term in Eq.33. Assuming that the normal tractions in the contact zone do not vary very much between the different adjacent "body" elements, which will be true in the case of exact contact enforcement, the necessary value of the normal traction can be taken from *any* of the adjacent "body" elements. Thus, in the presented contact formulation, only one *arbitrarily chosen* "body" element is considered for the computation of the necessary normal traction t_N (see Fig. 9). One may wonder if this arbitrary choice may lead to oscillations in the normal contact tractions, but the authors can report that no such problems were observed in the numerical examples presented in section 5.

Under this assumption, the discretized version of the stabilized, variational constraint Eq.41 can be decoupled and enforced separately for every single contact

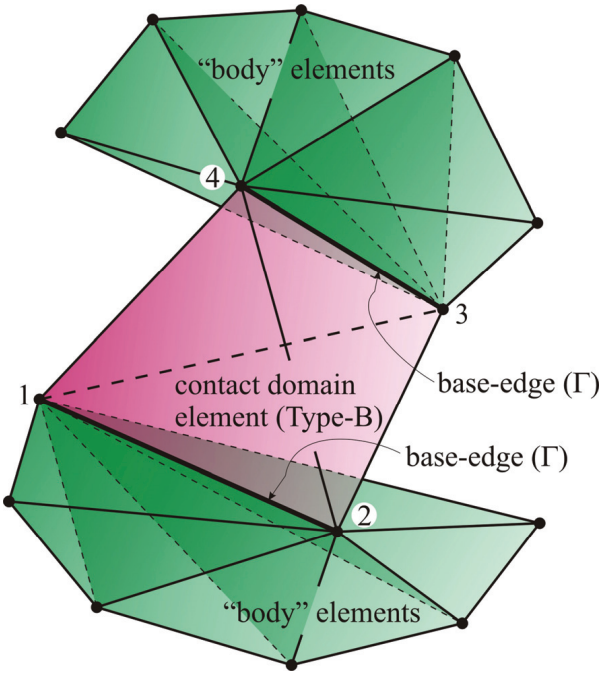

Figure 8: Contact domain patch (Type-B) with adjacent "body" elements

domain patch, similarly to Type-A patches. Now, the analytical integration of the stabilization term has to be performed along the common edge of the contact patch and the chosen adjacent "body" element. Using

$$\int_D dD = V = \frac{1}{3}A^* H \text{ and } \int_\Gamma d\Gamma = L_1 \tag{52}$$

and inserting into Eq.41 leads to

$$\frac{1}{3}A^* H \bar{g}_N + L_1 \tau \left(t_N - \Lambda_N\right) = 0 \quad \Rightarrow \quad \frac{1}{3}\frac{A^*}{L_1} H \bar{g}_N + \tau t_N = \tau \Lambda_N, \tag{53}$$

which can again directly be solved for the discrete normal Lagrange multiplier:

$$\Lambda_N = t_N + \frac{A^*}{L_1}\frac{H}{3\tau}\bar{g}_N \tag{54}$$

Expressing the normal gap intensity alternatively with

$$\bar{g}_N = \frac{g_N\left(\mathbf{x}_n\right)}{\left|G_N\left(\mathbf{x}_n\right)\right|} = \frac{g_{N,34}}{\left|G_{N,34}\right|} = \frac{g_{N,34}}{H} \tag{55}$$

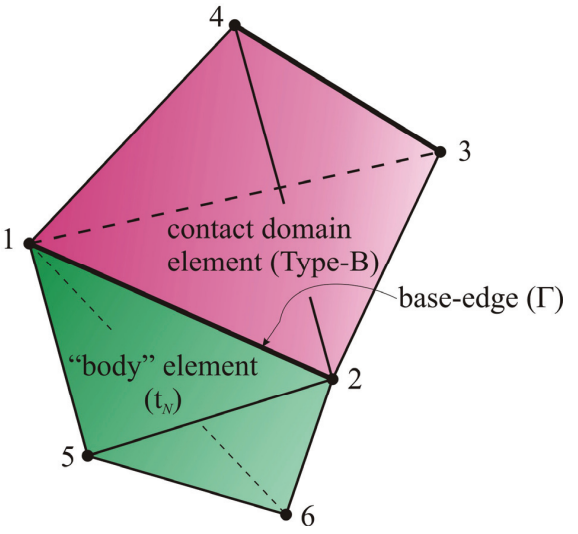

Figure 9: Contact domain patch (Type-B) with used adjacent "body" element for stabilization

Eq.54 can be simplified to

$$\Lambda_N = t_N + \frac{A^*}{L_1}\frac{1}{3\tau} g_{N,34} \tag{56}$$

As this expression is very similar to the one derived for Type-A patches in Eq.47, a constant c_1 and the normal gap of the contact patch $g_N^{(p)}$ will be introduced to get a consistent expression for the evaluation of the discrete normal Lagrange multiplier. It is given by

$$\Lambda_N = t_N + \frac{c_1}{3\tau} g_N^{(p)} \text{ with } \begin{cases} c_1 = 1.0 \text{ and } g_N^{(p)} = g_{N,4} & \text{for } Type-A \\ c_1 = \frac{A^*}{L_1} \text{ and } g_N^{(p)} = g_{N,34} & \text{for } Type-B \end{cases} \tag{57}$$

3.3 Contact contributions

Once the discrete normal Lagrange multipliers have been determined (see Eq.57), enforcing the local contact constraints (see sections 3.1.2 and 3.2.2), the resulting contact contributions can be calculated. Therefore the contact virtual work expression Eq.32 is discretized, using the mentioned approximations. The evaluation of the contact virtual work necessitates the variation of the normal gap intensity

$$\delta \bar{g}_N = \bar{g}_N \mathbf{n} \cdot grad\,(\delta \mathbf{u}) \cdot \mathbf{n}, \tag{58}$$

derived in Appendix A, which turns out to be constant within one contact domain patch as well. Thus, the necessary integration of the discretized contact virtual work equation can be performed analytically using Eq.40 and Eq.49, respectively. This leads to

$$\delta\Pi_{cont}^{(h)} = \frac{1}{3}AH\Lambda_N\bar{g}_N\mathbf{n}\cdot grad\,(\delta\mathbf{u})\cdot\mathbf{n} = \frac{A}{3}\Lambda_N g_N^{(p)}\mathbf{n}\cdot grad\,(\delta\mathbf{u})\cdot\mathbf{n} \tag{59}$$

wherein Eq.46 and Eq.57 have been used. Inserting the linear discretization of the displacement field within a contact domain element in Eq.4, this can be rewritten as

$$\delta\Pi_{cont}^{(h)} = \frac{A}{3}\Lambda_N\mathbf{n}\cdot\sum_{I=1}^{4}\left(g_N^{(p)}\frac{\partial N_I}{\partial n}\right)\cdot\delta\mathbf{d}_I \tag{60}$$

where $\frac{\partial N_I}{\partial n}$ is the derivative of the shape function N_I with respect to the arclength n along the current normal direction $\mathbf{n}$. The evaluation of the expressions given in brackets in Eq.60 can be done based on geometrical properties of a contact domain patch, regardless of the value of the actual geometrical normal gap $g_N^{(p)}$, which will be shown in the following.

3.4 Normal direction derivatives

3.4.1 Type-A contact patch

In Fig. 10a) a geometrical interpretation of the normal direction derivative of the first shape function N_1 is shown for a Type-A contact patch. Multiplying the shape function with the geometrical normal gap ($g_{N,4} = g_N^{(p)}$) of vertex node 4 allows for a direct evaluation of the terms

$$g_N^{(p)}\frac{\partial N_1}{\partial n} = -\frac{a_1}{l_1};\;\; g_N^{(p)}\frac{\partial N_2}{\partial n} = -\frac{a_2}{l_2};\;\; g_N^{(p)}\frac{\partial N_3}{\partial n} = -\frac{a_3}{l_3};\;\; g_N^{(p)}\frac{\partial N_4}{\partial n} = 1. \tag{61}$$

It is only necessary to get the ratios of how the normal projection of node 4 intersects the base-face triangle, defined by the vertex nodes 1, 2 and 3 (see Fig. 10b)).

3.4.2 Type-B contact patch

In Fig. 11 a geometrical interpretation of the normal direction derivatives is shown for a Type-B contact patch. Multiplying the shape functions with the geometrical normal gap ($g_{N,34} = g_N^{(p)}$) of the vertex nodes 3 and 4 allows for a direct evaluation

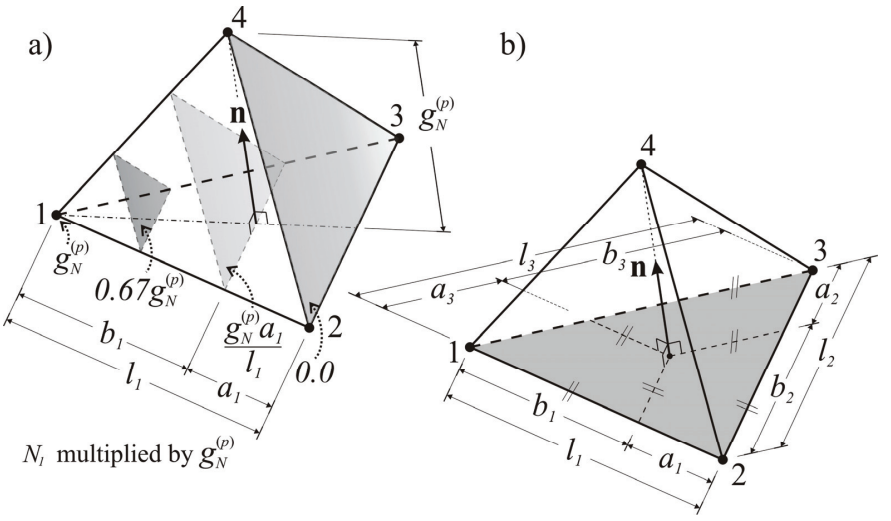

Figure 10: Normal direction derivatives for a Type-A patch

of the terms

$$\begin{aligned} g_N^{(p)}\frac{\partial N_1}{\partial n} &= -\frac{a_1}{l_1}; \quad g_N^{(p)}\frac{\partial N_2}{\partial n} = -\frac{b_1}{l_1}; \\ g_N^{(p)}\frac{\partial N_3}{\partial n} &= +\frac{a_2}{l_2}; \quad g_N^{(p)}\frac{\partial N_4}{\partial n} = +\frac{b_2}{l_2}. \end{aligned} \tag{62}$$

Again, it is only necessary to get the ratios of how the normal projection of the edges 1-2 and 3-4 intersect each other to find the corresponding values in Eq.62.

Remark 3.2. Notice that the evaluation of the contact virtual work in Eq.60 is independent of the elemental normal gap $g_N^{(p)}$, as the necessary normal direction derivatives can be computed on the basis of pure geometrical properties of the considered contact patch (see Eq.61 and Eq.62). This in turn implies that the discrete contact virtual work expression Eq.59 can be determined independently of the initial normal gap $G_N(\mathbf{x}_n)$, which could eventually be null, without ill conditioning the problem (see Remark 2.5).

3.5 Linearization of contact contributions

To solve the resulting discretized set of non-linear equations, a classical Newton-Raphson scheme is employed, which, in order to guarantee a quadratic convergence near the solution, necessitates the construction of the effective tangential stiffness

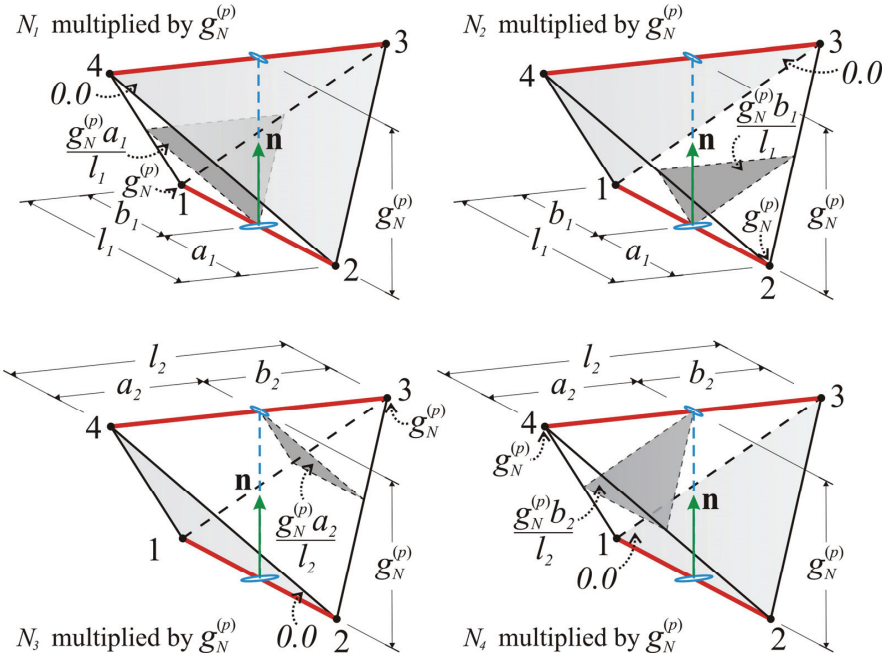

Figure 11: Normal direction derivatives for a Type-B patch

matrix. The construction of this tangent stiffness requires, amongst others, the linearization of the contact virtual work expression Eq.32, which can be written as

$$\Delta\delta\Pi_{cont} = \int_{D_n^{(N)}} \Delta\lambda_N \delta\bar{g}_N \, dD + \int_{D_n^{(N)}} \lambda_N \Delta\delta\bar{g}_N \, dD \tag{63}$$

Introducing the specified approximations for the normal Lagrange multiplier from Eq.34 and performing the analytical integration using Eq.42 and Eq.49, respectively, the discretized version of Eq.63 can be written for one contact domain element as

$$\Delta\delta\Pi_{cont} = \frac{A}{3} H \left(\Delta\Lambda_N \delta\bar{g}_N + \Lambda_N \Delta\delta\bar{g}_N \right) \tag{64}$$

Its evaluation necessitates the linearization of the discrete normal Lagrange multi-

plier $\Delta\Lambda_N$ and the linearization of the variation of the normal gap intensity

$$\Delta\delta\bar{g}_N = -\bar{g}_N\left[t^{\alpha\beta}\left(\mathbf{n}\cdot\frac{\partial\delta\mathbf{u}}{\partial t_\alpha}\right)\left(\mathbf{n}\cdot\frac{\partial\Delta\mathbf{u}}{\partial t_\beta}\right)+t^{\alpha\beta}\left(\mathbf{n}\cdot\frac{\partial\delta\mathbf{u}}{\partial t_\alpha}\right)\left(\mathbf{t}_\beta\cdot\frac{\partial\Delta\mathbf{u}}{\partial n}\right)+t^{\alpha\beta}\left(\mathbf{t}_\alpha\cdot\frac{\partial\delta\mathbf{u}}{\partial n}\right)\left(\mathbf{n}\cdot\frac{\partial\Delta\mathbf{u}}{\partial t_\beta}\right)\right] \quad (65)$$

which is derived in Appendix A. Herein, $\mathbf{t}_\alpha$ ($\alpha = 1,2$) are the covariant tangent vectors in the current configuration and $t^{\alpha\beta}$ is the contravariant metric tensor, corresponding to the coordinate system defined by $\mathbf{t}_1$, $\mathbf{t}_2$ and $\mathbf{n}$. Using Eq.46 and Eq.57, the linearization of the discrete normal Lagrange multiplier yields

$$\Delta\Lambda_N = \Delta t_N + c_1\frac{H}{3\tau}\Delta\bar{g}_N \quad (66)$$

where the linearization of the normal gap intensity has the same structure as its variation in Eq.58:

$$\Delta\bar{g}_N = \bar{g}_N\mathbf{n}\cdot grad\,(\Delta\mathbf{u})\cdot\mathbf{n} \quad (67)$$

All terms discussed so far depend upon the displacements of the vertices of one contact domain element. However, the linearization of the normal contact traction Δt_N depends upon the displacement and the constitutive behavior of the adjacent "body" element, used for the stabilization of the variational constraint equation (see section 3.1.2 and Fig. 6 for Type-A and section 3.2.2 and Fig. 9 for Type-B contact patches). This involves additional degrees of freedom of finite element nodes in the interior of the contacting bodies. One additional node is necessary for Type-A patches (see Fig. 6, node 5) and two additional finite element nodes are needed in case of Type-B contact patches (see Fig. 9, nodes 5 and 6). Starting from Eq.15, the linearization of the normal contact traction yields

$$\Delta t_N = \Delta\mathbf{n}\cdot\mathbf{P}\cdot\mathbf{N}+\mathbf{n}\cdot\Delta\mathbf{P}\cdot\mathbf{N}, \quad (68)$$

where the linearization of the patch-wise constant normal vector in the current configuration is given by

$$\begin{aligned}\Delta\mathbf{n} &= -t^{\alpha\beta}\left(\mathbf{t}_\alpha\otimes\mathbf{n}\right)\cdot\frac{\partial\Delta\mathbf{u}}{\partial t_\beta} = -t^{\alpha\beta}\left(\mathbf{n}\cdot grad\,(\Delta\mathbf{u})\cdot\mathbf{t}_\beta\right)\mathbf{t}_\alpha\\ &= -\left(\mathbf{n}\cdot grad\,(\Delta\mathbf{u})\cdot\mathbf{t}_\alpha\right)t^\alpha.\end{aligned} \quad (69)$$

The derivation of this expression as well as the linearization of the first Piola-Kirchhoff stress tensor are detailed in Appendix A and B. Inserting Eq.69 into

Eq.68 gives

$$\Delta t_N = -\mathbf{t}^\alpha \cdot \mathbf{P} \cdot \mathbf{N} \left(\mathbf{n} \cdot \frac{\partial \Delta \mathbf{u}}{\partial t_\alpha} \right) + \mathbf{n} \cdot \Delta \mathbf{P} \cdot \mathbf{N} \tag{70}$$

Looking at Eq.70 it is obvious that the first term solely involves degrees of freedom of the contact domain patch and only the second term involves some degrees of freedom in the interior of the contacting bodies. To point this out, the linearization of the contact contributions in Eq.63 will be split into two parts

$$\Delta\delta\Pi_{cont} = \Delta\delta^I\Pi_{cont} + \Delta\delta^{II}\Pi_{cont} \tag{71}$$

where part one only affects degrees of freedom within a contact domain patch and part two additionally affects the degrees of freedom of the adjacent "body" element. The two parts can then be specified by

$$\Delta\delta^I\Pi_{cont} = \frac{A}{3} H \left(\underbrace{-(\mathbf{t}^\alpha \cdot \mathbf{P} \cdot \mathbf{N}) \left(\mathbf{n} \cdot \frac{\partial \Delta \mathbf{u}}{\partial t_\alpha} \right) \delta \bar{g}_N}_{non-symmetric} + c_1 \frac{H}{3\tau} \underbrace{\Delta \bar{g}_N \delta \bar{g}_N}_{symmetric} + \underbrace{\Lambda_N \Delta \delta \bar{g}_N}_{symmetric} \right) \tag{72}$$

and

$$\Delta\delta^{II}\Pi_{cont} = \frac{A}{3} H \underbrace{\mathbf{n} \cdot \Delta \mathbf{P} \cdot \mathbf{N} \delta \bar{g}_N}_{non-symmetric}. \tag{73}$$

From Eq.72 and Eq.73, it is obvious that the resulting contact stiffness matrix will comprise some non-symmetric parts, which are a direct result from the added stabilization term in the variational constraint Eq.33 (see also Remark 3.3 and [Oliver, Hartmann, Cante, Weyler and Hernández (2009)] for a more detailed discussion).

3.6 Matrix notation

In the following, a matrix notation will be introduced to compute the contact residual as well as the resulting contact stiffness matrix for one contact domain patch. It has been shown in the previous section that the linearization of the contact contributions will also affect some degrees of freedom of the utilized adjacent "body" element. Depending on the considered contact domain element, either one (node 5 for Type-A patches, see Fig. 6) or two (nodes 5 and 6 for Type-B patches, see Fig. 9) additional vertices in the interior of the contacting bodies need to be taken into

account. In order to get a compact matrix notation, a vector containing the variated nodal values

$$\delta \mathbf{d}_p^T = (\delta \mathbf{d}_1, \delta \mathbf{d}_2, \delta \mathbf{d}_3, \delta \mathbf{d}_4) \tag{74}$$

and two vectors containing the incremental nodal displacements

$$\begin{aligned} &\Delta^I \mathbf{d}_p^T = (\Delta \mathbf{d}_1, \Delta \mathbf{d}_2, \Delta \mathbf{d}_3, \Delta \mathbf{d}_4) \text{ and} \\ &\Delta^{II} \mathbf{d}_p^T = \begin{cases} (\Delta \mathbf{d}_1, \Delta \mathbf{d}_3, \Delta \mathbf{d}_2, \Delta \mathbf{d}_5) \text{ for Type - A patches} \\ (\Delta \mathbf{d}_1, \Delta \mathbf{d}_2, \Delta \mathbf{d}_5, \Delta \mathbf{d}_6) \text{ for Type - B patches} \end{cases} \end{aligned} \tag{75}$$

are defined, based on the five and six vertex/nodes indicated in Fig. 6 and Fig. 9, respectively. Furthermore, the following matrices will be defined:

$$\mathbf{N}_n = \begin{pmatrix} g_N^{(p)} \frac{\partial N_1}{\partial n} \mathbf{n} \\ g_N^{(p)} \frac{\partial N_2}{\partial n} \mathbf{n} \\ g_N^{(p)} \frac{\partial N_3}{\partial n} \mathbf{n} \\ g_N^{(p)} \frac{\partial N_4}{\partial n} \mathbf{n} \end{pmatrix}; \quad \mathbf{N}_{t\alpha} = \begin{pmatrix} \frac{\partial N_1}{\partial t_\alpha} \mathbf{n} \\ \frac{\partial N_2}{\partial t_\alpha} \mathbf{n} \\ \frac{\partial N_3}{\partial t_\alpha} \mathbf{n} \\ \frac{\partial N_4}{\partial t_\alpha} \mathbf{n} \end{pmatrix}; \quad \mathbf{T}_n^\alpha = \begin{pmatrix} g_N^{(p)} \frac{\partial N_1}{\partial n} \mathbf{t}^\alpha \\ g_N^{(p)} \frac{\partial N_2}{\partial n} \mathbf{t}^\alpha \\ g_N^{(p)} \frac{\partial N_3}{\partial n} \mathbf{t}^\alpha \\ g_N^{(p)} \frac{\partial N_4}{\partial n} \mathbf{t}^\alpha \end{pmatrix} \tag{76}$$

Herein, $g_N^{(p)} \frac{\partial N_I}{\partial n}$ are the normal direction derivatives given in Eq.61 and Eq.62, and $\mathbf{n}$ and $\mathbf{t}^\alpha$ are the patch-wise constant unit normal vector and the contravariant base vectors (not normalized) in the current configuration. Furthermore, $\frac{\partial N_I}{\partial t_\alpha}$ represents the derivatives of the linear shape functions with respect to the current (not normalized) covariant base vectors, which can be specified as follows:

$$\begin{aligned} &\text{Type - A patch: } \begin{cases} \frac{\partial N_1}{\partial t_1} = -1; & \frac{\partial N_2}{\partial t_1} = +1; & \frac{\partial N_3}{\partial t_1} = 0; & \frac{\partial N_4}{\partial t_1} = 0 \\ \frac{\partial N_1}{\partial t_2} = -1; & \frac{\partial N_2}{\partial t_2} = 0; & \frac{\partial N_3}{\partial t_2} = +1; & \frac{\partial N_4}{\partial t_2} = 0 \end{cases} \\ &\text{Type - B patch: } \begin{cases} \frac{\partial N_1}{\partial t_1} = -1; & \frac{\partial N_2}{\partial t_1} = +1; & \frac{\partial N_3}{\partial t_1} = 0; & \frac{\partial N_4}{\partial t_1} = 0 \\ \frac{\partial N_1}{\partial t_2} = 0; & \frac{\partial N_2}{\partial t_2} = 0; & \frac{\partial N_3}{\partial t_2} = +1; & \frac{\partial N_4}{\partial t_2} = -1 \end{cases} \end{aligned} \tag{77}$$

Finally the matrix $\mathbf{N}_{\sigma P}^T$, for computing the second part of the linearization of the discrete normal Lagrange multiplier (see Eq.70)

$$\mathbf{n} \cdot \Delta \mathbf{P} \cdot \mathbf{N} = \mathbf{N}_{\sigma P}^T \, \Delta^{II} \mathbf{d}_p \tag{78}$$

is given by

$$\mathbf{N}_{\sigma P}^T = \bar{\mathbf{N}} \left(\bar{\mathbf{S}} \, \tilde{\mathbf{B}} + \bar{\mathbf{F}} \, \mathbf{D} \, \mathbf{B} \right), \tag{79}$$

where the vector

$$\bar{\mathbf{N}} = \begin{pmatrix} n_1N_1 & n_2N_2 & n_3N_3 & n_1N_2 & n_2N_1 & n_2N_3 & n_3N_2 & n_1N_3 & n_3N_1 \end{pmatrix} \tag{80}$$

contains the products of the components of the current and the previous normal vectors. The remaining matrices needed in Eq.79 are introduced and detailed in Appendix B.

With the vectors and matrices defined in Eqs.74-78, the contact virtual work done by one contact patch (Eq.60) can be written in matrix formulation $\delta\mathbf{d}^T\mathbf{G}_{cont}$ with the elemental contact residual

$$\mathbf{G}_{cont} = \frac{A}{3}\Lambda_N\mathbf{N}_n. \tag{81}$$

Furthermore the linearization of the contact contributions Eq.72 and Eq.73 leads to

$$\Delta\delta^I\Pi_{cont} + \Delta\delta^{II}\Pi_{cont} = \delta\mathbf{d}^{TI}\mathbf{K}_{cont}\Delta^I\mathbf{d} + \delta\mathbf{d}^{TII}\mathbf{K}_{cont}\Delta^{II}\mathbf{d}, \tag{82}$$

with the elemental contact stiffness matrices

$$\begin{aligned} {}^I\mathbf{K}_{cont} = -\frac{A}{3}\Lambda_N\left(g_n^{(p)}t^{\alpha\beta}\mathbf{N}_{t\alpha}\mathbf{N}_{t\beta}^T + \mathbf{T}_n^\alpha\mathbf{N}_{t\alpha}^T + \mathbf{N}_{t\alpha}\mathbf{T}_n^{\alpha T}\right) + \frac{A}{9\tau}c_1\mathbf{N}_n\mathbf{N}_n^T \\ - \frac{A}{3}\left(\mathbf{t}^\alpha\cdot\mathbf{P}\cdot\mathbf{N}\right)\mathbf{N}_n\mathbf{N}_{t\alpha}^T \end{aligned} \tag{83}$$

and

$${}^{II}\mathbf{K}_{cont} = \frac{A}{3}\mathbf{N}_n\mathbf{N}_{\sigma P}^T. \tag{84}$$

Remark 3.3. Looking at the contact stiffness matrices derived in this section, it becomes obvious that they exhibit non-symmetric parts. These parts stem from the introduction of the additional (stabilization) terms solely in the constrained variational Eqs.33. Although Heintz and Hansbo (2006) have proposed a consistent symmetric version of stabilization, the authors have decided to add the stabilization terms only in the constrained equations, since future work will be dedicated to incorporate friction laws to the presented contact strategy, which will lead to non-symmetric parts in the contact stiffness matrix anyway.

4 Active set strategy

It was already stated in section 2.8 that in this work an active set strategy is employed in order to translate the initial inequality constrained problem into an equality constrained one. In the following, the basic ideas of a predictive active set

strategy, which have been introduced and applied successfully in two-dimensional contact problems in [Oliver, Hartmann, Cante, Weyler and Hernández (2009)] and [Hartmann, Oliver, Weyler, Cante and Hernández (2009)], will be recalled. Furthermore, important technical aspects, which are especially crucial in three-dimensional analysis, will be presented.

4.1 Effective normal gap and active constraint indicator

Considering the discrete constraint enforcement derived in sections 3.1.2 and 3.2.2 for Type-A and Type-B patches, respectively, the actual numerical constraint (see Eq.57)

$$g_N^{(p)} + \frac{3\tau^{(p)}}{c_1}\left(t_N - \Lambda_N^{(p)}\right) = 0 \tag{85}$$

can be extracted. This constraint represents the numerical counterpart of the geometrical impenetrability condition, saying that the actual normal gap has to be closed, once there is contact between two deformable bodies. From Eq.85 it is obvious that the discrete numerical impenetrability condition is computed as the sum of the actual elemental normal gap $g_N^{(p)}$ plus an additional term $(t_N - \Lambda_N^{(p)})$ penalized by the stabilization parameter $\tau^{(p)}$. That is why the left hand side of Eq.85 has been considered the so-called *numerical normal gap*

$$g_N^{num.(p)} = g_N^{(p)} + \frac{3\tau^{(p)}}{c_1}\left(t_N - \Lambda_N^{(p)}\right) \tag{86}$$

in [Oliver, Hartmann, Cante, Weyler and Hernández (2009)].

Remark 4.1. A null value of $\tau^{(p)}$ will translate into a numerical normal gap which is equal to the geometrical normal gap, and, therefore, into an exact imposition of the impenetrability condition within a contact patch p. Small non-zero values of $\tau^{(p)}$, necessary for the lambda-solvability issues, will perturb slightly that exact imposition of the geometrical constraints. Additionally, mesh refinement will also make the penalized terms $(t_N - \Lambda_N^{(p)})$ tend to zero, according to Eq.24, and, again, the numerical and geometrical gaps will coincide, regardless of the size of the penalty value $\tau^{(p)}$ (consistent penalty).

With the definition of the numerical normal gap in Eq.86 and accounting for the discrete constraint Eq.85, one can solve for the discrete local normal Lagrange multiplier as described in sections 3.1.2 and 3.2.2 (see Eq.57). By multiplying Eq.57 times $3\tau^{(p)}/c_1$ one gets the so-called effective normal gap:

$$g_N^{eff.(p)} = g_N^{(p)} + \frac{3\tau^{(p)}}{c_1} t_N = \frac{3\tau^{(p)}}{c_1}\Lambda_N^{(p)}, \tag{87}$$

where the constant c_1 takes the values given in Eq.57, depending on the considered type of contact patch.

Remark 4.2. The most relevant features of the effective normal gap $g_N^{eff.(p)}$ defined in Eq.87 are:

- Since $\tau^{(p)} > 0$ *it has the same sign* as the discrete normal Lagrange multiplier $\Lambda_N^{(p)}$:

  $$sign\left(g_N^{eff.(p)}\right) = sign\left(\Lambda_N^{(p)}\right) \tag{88}$$

  Therefore, the effective normal gap is a *displacement-based* indicator of the sign of the normal Lagrange multiplier.

- It is constructed on the basis of the patch-wise constant geometrical normal gap $g_N^{(p)}$ and the normal contact traction t_N. Due to this, it exhibits suitable *smoothness properties* in situations involving change of the contact scenario, like contact-to-release. This fact will be crucially used in the specific algorithm for determining the active normal contact set.

According to the definition of the active normal contact domain $D_n^{(N)}$ in Eq.26, the values of the discrete normal Lagrange multiplier will be used to decide, whether a contact patch p belongs to $D_n^{(N)}$

$$\Lambda_N^{(p)} < 0 \;\Leftrightarrow\; D_n^{(p)} \subset D_n^{(N)} \quad \rightarrow \text{active normal contact} \tag{89}$$

Now, in view of Eq.88 and Eq.89, the effective normal gap may be obtained as a suitable *active constraint indicator* β_N:

$$D_n^{(p)} \subset D_n^{(N)} \quad \Leftrightarrow \quad \beta_N \equiv g_N^{eff.(p)} < 0 \quad \rightarrow \text{active normal contact} \tag{90}$$

4.2 Prediction of the active normal contact set

In the light of the experience in previous works [Oliver, Hartmann, Cante, Weyler and Hernández (2009); Hartmann, Oliver, Weyler, Cante and Hernández (2009)], the authors can report that the rate of convergence of the active contact set crucially depends on the appropriate prediction of the initial active contact set made in the first iteration. Therefore the active contact set in the first iteration is defined computing the active normal constrained indicator on basis of a first order extrapolation of its value at previous time steps:

$$\beta_N^{(1)} = \tilde{g}_N^{eff.(p)} \tag{91}$$

with

$$\tilde{g}_N^{eff.(p)}(t_{n+1}) = g_N^{eff.(p)}(t_n) + \frac{\Delta t_{n+1}}{\Delta t_n}\Delta g_N^{eff.(p)} \tag{92}$$

Herein Δt_{n+1} and Δt_n are the current and the previous time increments and $\Delta g_N^{eff.(p)}$ is the increment of the effective normal gap

$$\Delta g_N^{eff.(p)} = g_N^{eff.(p)}(t_n) - g_N^{eff.(p)}(t_{n-1})\,. \tag{93}$$

Details about the technical aspects of keeping track of the history of the effective normal gaps can be found in [Hartmann, Oliver, Weyler, Cante and Hernández (2009)] and will not be recalled in this work.

4.3 Verification of active normal contact set

One main difference of the present contact formulation with respect to more classical ones is the fact that the potential contact pairing is done via a constrained Delaunay tessellation (see section 2.3.1), which results in the discretization of the introduced contact domain via linear tetrahedral contact patches of Type-A and Type-B. Thus, no kind of projection algorithm is employed, like for example in classical node-to-surface contact algorithms, to check whether the normal projection of a certain slave-node will be contained in a considered master segment. An essential property of the presented contact domain method is the discretization of the contact domain with a full set of non-overlapping patches, which directly leads to some kind of "distorted" contact patches, having its normal projection out of the base-face (see Fig. 12).

But precisely this feature allows this strategy to exactly pass the contact patch test also in three dimensions, as will be shown in section 5.1. Taking into account the "distorted" contact patches is, on the one hand, necessary for the fulfilment of the contact patch test, but, on the other hand, their activation might be error prone in other contact scenarios, like the one shown in Fig. 13, implying an "unphysical" constraint: In this particular case, the Type-A contact domain patch would be activated due to the definition of the active constraint indicator in Eq.90, which is obviously the wrong choice, as the two bodies are not going to contact each other. Therefore some additional verifications of the initially defined active normal contact set have to be carried out. It has to be checked whether the activated contact patch will take part in a physically meaningful contact scenario, performing some kind of segment-to-segment projections. This will be explained in the following, individually for Type-A and Type-B patches.

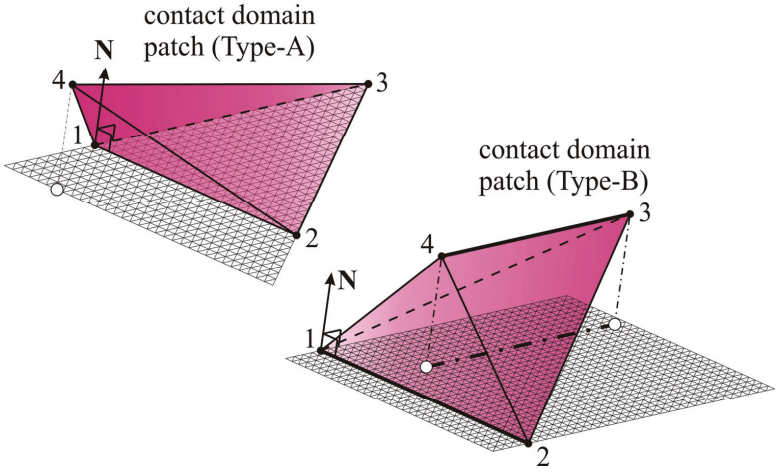

Figure 12: "Distorted" contact patches

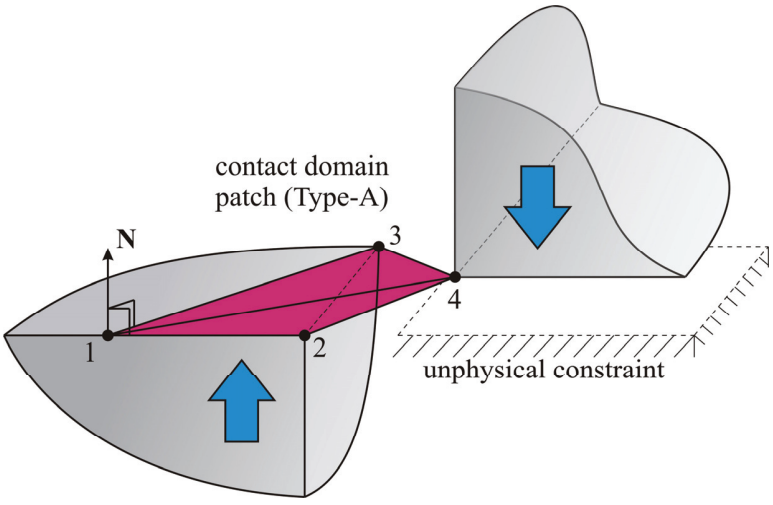

Figure 13: Contact scenario, which necessitates additional verification of active contact set

4.3.1 Segment-to-Segment projection check: Type-A patches

It is obvious that a physical contact can only take place when the contacting surfaces are really going to touch each other, which means that the projection of the discretized boundary faces need to overlap. Therefore, it is considered that a given Type-A contact patch can only participate actively in the contact when at least one of the adjacent boundary faces of its lonely vertex node 4 shares an overlapping region with the base-face of the contact patch (vertices 1,2,3), when projected onto its plane, using the patch-wise constant current normal direction **n**.

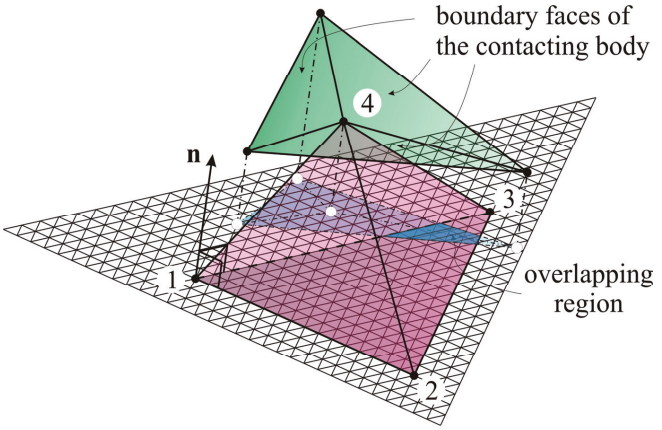

Figure 14: Projection of adjacent boundary faces onto base-plane for Type-A patch

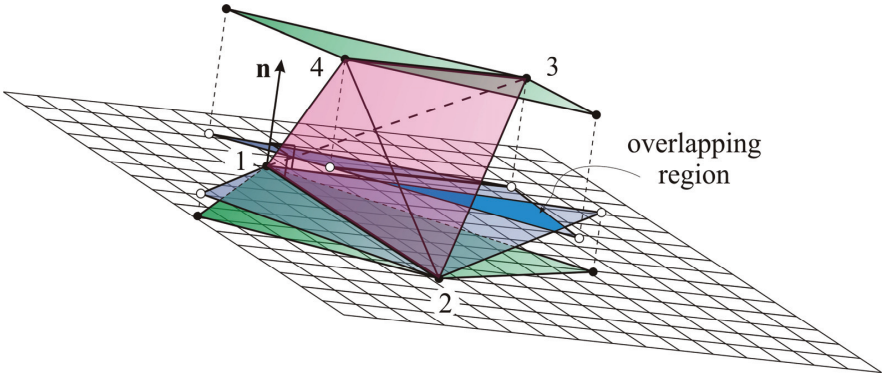

Figure 15: Projection of adjacent boundary faces for Type-B patch

In Fig. 14 a Type-A contact patch is shown together with the adjacent "body" boundary faces at the vertex node 4 and the projection of these faces onto the plane, defined by the vertex nodes 1, 2 and 3. In this particular case, the projected boundary faces share an overlapping region with the base-face and thus, this contact patch is considered to remain active after this check. Initially activated contact patches that do not pass this overlapping test will be deactivated and removed from the active contact set.

4.3.2 Segment-to-Segment projection check: Type-B patches

The strategy to eliminate unwanted Type-B contact patches from the active normal contact set is basically the same as for Type-A patches. Now it has to be checked, whether the two adjacent "body" boundary faces connected to either base-side of the Type-B contact patch will share some overlapping region, when they are projected onto each other using the patch-wise constant current normal direction $\mathbf{n}$. In contrast to Type-A patches, this normal generally is not perpendicular to any of the tested faces.

Remark 4.3. The verification of the active normal contact set, by means of the procedure described before, might seem to be quite expensive. However it has to be emphasized that these additional checks only need to be performed if the considered contact patch satisfies the following two conditions:

- It has been detected as part of the active normal contact set through the condition in Eq.90.
- It displays a "distorted" patch, which equivalently is characterized by the fact that at least one of the normal direction derivatives computed with Eq.61 and Eq.62, respectively, fulfill the criteria

$$\left| g_N^{(p)} \frac{\partial N_I}{\partial n} \right| > 1.0. \tag{94}$$

Therefore the number of contact patches that needs to be subjected to the aforementioned projection checks is very limited and thus the additional numerical cost becomes negligible.

4.4 Iterative solution algorithm

The iterative solution algorithm, focussing on the update of the active contact set is shown in Box 1 for the current time step $[t_n, t_{n+1}]$. Herein $\mathbf{K}_T\left(\mathbf{d}^{(i)}\right)$ and $\mathbf{G}\left(\mathbf{d}^{(i)}\right)$ represent the global tangent stiffness matrix and the residual vector of the linearized problem, including the deformable bodies as well as the contact part described in

section 3.6. All the unknown incremental nodal displacements at iteration i are concentrated in the vector $\Delta\mathbf{d}^{(i)}$. As can be seen from the algorithm in section 3.6, the update of the active normal contact set is performed within each step of the NEWTON iteration in order to accelerate the total solution procedure.

5 Numerical examples

Various numerical examples have been chosen to demonstrate the performance of the proposed contact strategy. All the examples are computed employing a compressible neo-Hookean, hyperelastic constitutive law [Bonet and Wood (1997)], which is determined by the Young's modulus E and the Poisson's ratio ν. Furthermore, the following relation for the patch-wise constant stability parameter τ in Eq.33 will be used.

$$\begin{cases} \tau = \frac{\alpha_{\text{stab}}}{E_{\min}} \sqrt{A} & \text{for Type - A} \\ \tau = \frac{1}{4} \frac{\alpha_{\text{stab}}}{E_{\min}} \left(L_1 + L_2\right)^2 & \text{for Type - B} \end{cases} \tag{95}$$

Herein, $E_{\min}$ is the minimal Young's modulus of the contacting bodies, A, L_1 and L_2 represent the base-face area of a Type-A contact patch (see Eq.39) and the two base-side lengths of a Type-B contact patch (see Eq.51) in the previous configuration, respectively, and α_{stab} is a dimensionless, user defined parameter, which is independent of the mesh-size. The distinction between Type-A and Type-B patches in Eq.95 is necessary, due to the fact that the integration of the additional stabilization term in Eq.33 is either performed over an area (Type-A patches) or along a line (Type-B patches). From compatibility reasons of the units in the variational constraint equation, the stabilization parameter τ needs to be $\left[m^3/N\right]$ in case of Type-A patches and $\left[m^4/N\right]$ in case of Type-B patches. Furthermore, a suitable value of the stabilization parameter τ is governed by the present stresses in the contact interface which, in turn, depend upon the Young's modulus. Finally the stabilization parameter τ needs to be adjusted with the characteristic size of a contact domain element.

5.1 Contact patch test

A contact formulation should be able to exactly transmit a spatially constant stress field from one body to another along an arbitrary non-conforming contact surface. This ability will be checked by the so-called contact patch test [Laursen (2002)]. The test setup is chosen according to [Puso and Laursen (2004a)]. Two identical cubes with edge length $l = 12\,mm$ and elastic material properties ($E = 1.0\,N/mm^2$, $\nu = 0.3$) are uniaxially compressed by a uniform prescribed vertical displacement applied to the top surface of the upper cube. Fig. 16a) and b) show

LOOP over NEWTON ITERATION: $i = 1, ..., convergence$

LOOP over all contact patches p

IF $(i = 1)$ THEN

Define the potential ACTIVE SET based on extrapolated indicators

$\beta_N^{(1)} = \tilde{g}_N^{eff.(p)}$

ELSE IF $(i > 1)$

Define the potential ACTIVE SET based on updated indicators

$\beta_N^{(i)} = \beta_N(\mathbf{d}^{(i)})$

END IF

IF $\left(\beta_N^{(i)} < 0 \ .AND. \ any \left| g_N^{(p)} \frac{\partial N_I}{\partial n} \right| > 1.0 \right)$ THEN

Perform Segment-to-Segment projection check (section 4.3)

IF (no overlap) THEN

Remove p from the active set: $\beta_N^{(i)} > 0$

END IF

END IF

IF $\beta_N^{(i)} < 0$ THEN

$D_n^{(p)} \subset D_n^{(N)}$

END IF

END LOOP over contact patches

Solve the equality constrained problem

$\mathbf{K}_T\left(\mathbf{d}^{(i)}\right)\Delta\mathbf{d}^{(i)} = -\mathbf{G}\left(\mathbf{d}^{(i)}\right)$

Update incremental displacements

$\mathbf{d}^{(i+1)} = \mathbf{d}^{(i)} + \Delta\mathbf{d}^{(i)}$

Check for convergence: $\left\|\mathbf{G}\left(\mathbf{d}^{(i+1)}\right)\right\| \leq TOL \ \Rightarrow$ STOP

END LOOP over NEWTON ITERATION

Box 1: Solution algorithm with active set strategy for one time step

the finite element mesh in the contact interface, which clearly demonstrates the non-conforming character. The contour plot of the vertical stresses is depicted in Fig. 16c), displaying a completely homogeneous stress state, thus verifying that the present contact strategy exactly passes the contact patch test. It can be reported that a crucial point of this ability is the usage of a full set of non-overlapping contact patches (covering completely the contact domain), including both Type-A and Type-B patches. Furthermore it is worth noting that this result is totally independent of the used value of the stabilization parameter α_{stab}. This is due to the fact that in this particular example, the geometrical impenetrability condition can be exactly satisfied, as the contact interface is perfectly flat.

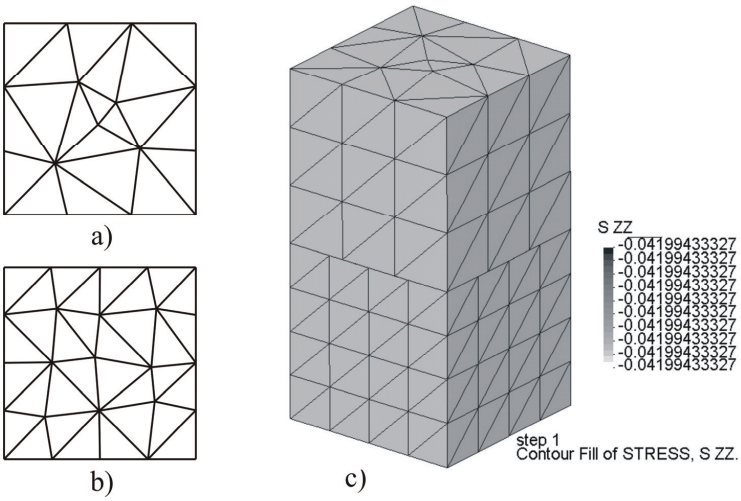

Figure 16: Contact patch test: a) Upper surface mesh; b) lower surface mesh; c) contour plot of vertical stresses

5.2 Hertzian contact

To demonstrate the accuracy of the proposed contact strategy the contact of an infinite linear-elastic half-cylinder is investigated. The half-cylinder is situated on a flat rigid foundation and its top surface is loaded by a constant pressure p. Since the analytical solution is based on the assumption of infinitesimal small deformations, a very small load is applied. The geometry, the material properties and the applied load are chosen in accordance to [Hartmann (2007); Popp, Gee and Wall (2009); Yang, Laursen and Meng (2005)] and can be extracted from Fig. 17.

The analytical solution for the contact traction is based on the classical Hertzian

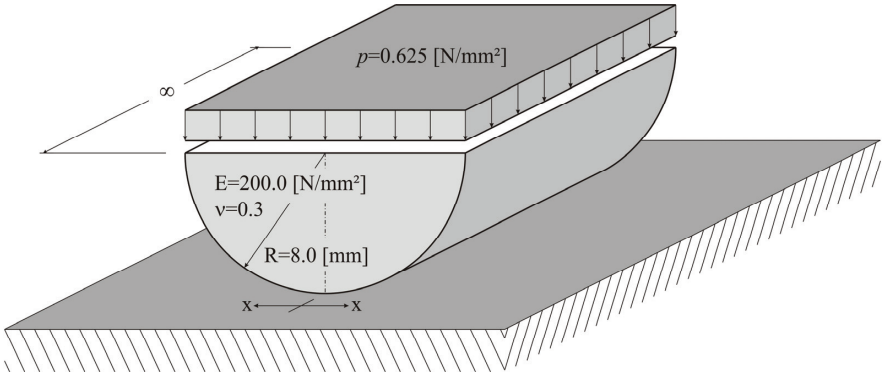

Figure 17: Hertzian contact: Geometry, material and loading

theory and can be found in [Kikuchi and Oden (1988)]:

$$t_N = \frac{4Rp}{\pi b^2}\sqrt{b^2 - x^2} \text{ with } b = 2\sqrt{\frac{2R^2 p\,(1-\nu^2)}{E\pi}} \tag{96}$$

Herein, b denotes the half width of the contact zone, R is the radius of the half-cylinder and x displays the control variable, starting from the axis of the half-cylinder (see Fig. 17). For the given set of parameters, the contact zone is determined with $b = 0.6808\,mm$. Due to the infinite dimension in longitudinal direction, this problem could be analyzed under the assumption of a plane strain condition, using a two-dimensional model. This has been done in the aforementioned papers. However, in this work, the accuracy of the presented three-dimensional contact formulation is analyzed, modeling a transversally constrained slice of the infinite half-cylinder, by applying the appropriate displacement boundary conditions to it. Furthermore, due to the symmetry of the problem, only one half of the half-cylinder is discretized with 4-noded, linear tetrahedral finite elements. A comparison is supplied for a coarse mesh with 6000 finite elements (shown in Fig. 18 together with the applied boundary conditions) and a finer mesh with 96000 elements (not shown), while using a stabilization parameter of $\alpha_{\text{stab}} = 0.01$.

The results of the analyses are shown in Fig. 19, where the horizontal lines represent the constant value of the normal contact traction along the face of a contact domain patch. Therefore, the analytical solution of the contact traction can only be represented by a stepwise constant characteristic. However, even the course mesh is able to capture the correct maximum value of the normal contact tractions. The results with the finer discretization converge nicely to the expected analytical

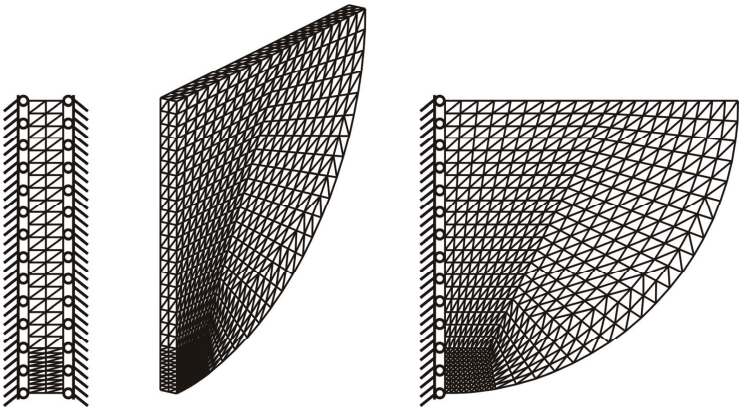

Figure 18: Hertzian contact: finite element discretization (course mesh) and boundary conditions

solution.

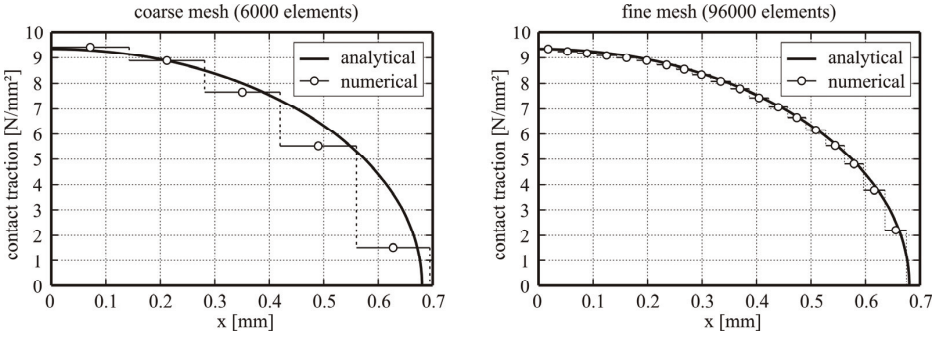

Figure 19: Hertzian contact: Coarse and fine mesh results

5.3 Ironing

This example was analyzed by Puso and Laursen (2004a) to demonstrate the performance of their mortar segment-to-segment contact strategy. A cylindrical die is first pressed vertically into a softer slab and then slid horizontally over it. The movement of the die is superimposed by prescribed displacement boundary conditions applied to the surface lines marked with A, B and C in Fig. 20. From time $0.0-0.2\,s$ the die is vertically displaced by $u_V = 1.5\,mm$ and then it travels hori-

zontally $u_H = 4.0\,mm$ from time $0.2 - 1.5\,s$. The geometry, the material properties as well as the boundary conditions of the ironing problem are shown in Fig. 20. In the numerical analysis, a constant time step size of $\Delta t = 0.01\,s$ has been used and the stabilization parameter was set to $\alpha_{\text{stab}} = 0.01$.

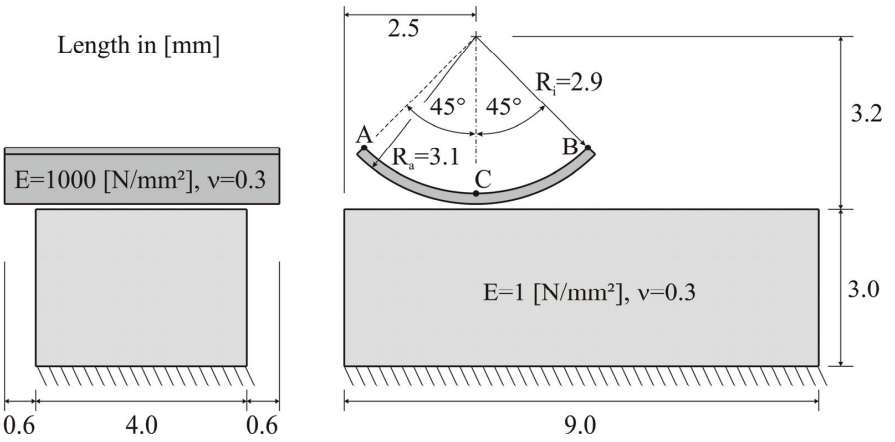

Figure 20: Ironing: Geometry, material data and boundary conditions

The employed discretization together with the initial and three deformed configurations of the computation are shown in Fig. 21, which demonstrate the finite deformations involved in this ironing process. In [Puso and Laursen (2004a)] it was reported that a standard node-on-segment contact algorithm could not achieve convergence, to any degree, on any of the meshes they have used. With the presented contact domain method, the analysis could be easily run up to the end.

5.4 Wavy cylinder

This example has been investigated to demonstrate the capability of the presented contact pairing strategy, described in section 2.3.1, to automatically handle self-contact scenarios without any further modification. A wavy cylinder is fixed at the bottom and compressed by a prescribed vertical displacement at the top. The geometry, the material data and the applied boundary conditions are given in Fig. 22. A maximum vertical displacement $u_V = 100\,mm$ is applied in 40 time steps, using a stabilization parameter $\alpha_{\text{stab}} = 0.01$.

In Fig. 23 the initial as well as three deformed configurations of this problem are shown, which nicely demonstrate the presence of self-contact on either side of the cylinder wall. Thus, in contrast to many other contact pairing algorithms, the

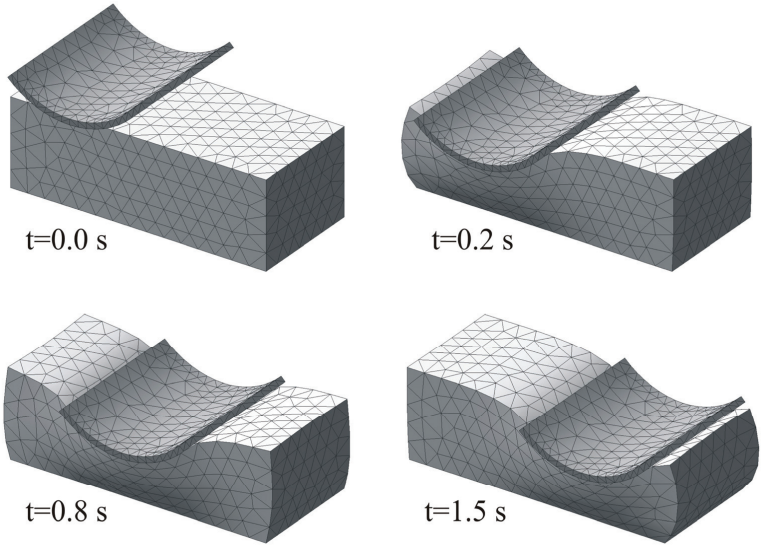

Figure 21: Ironing: Deformed configurations at different time steps

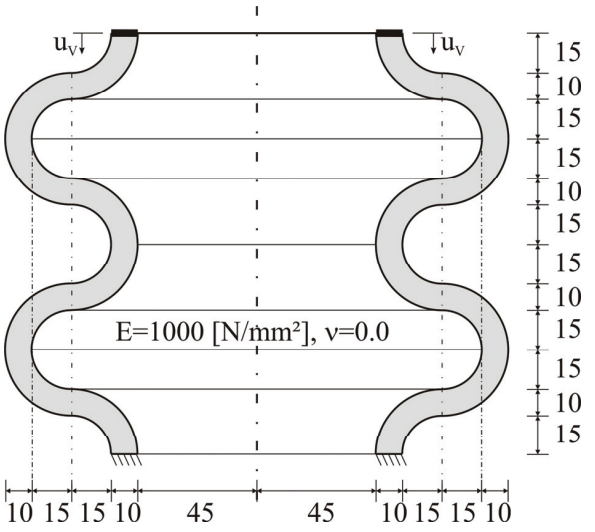

Figure 22: Wavy cylinder: Geometry, material data and boundary conditions

presented pairing strategy based on a constrained Delaunay tessellation constitutes a general tool that can handle any type of contact scenarios, including self-contact, without any additional modifications.

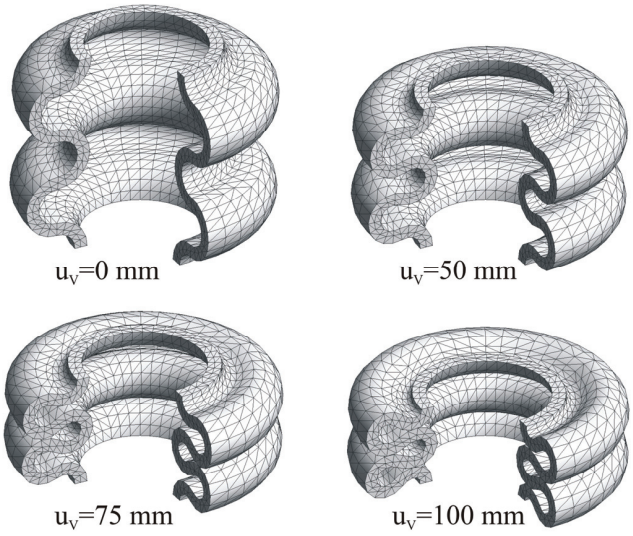

Figure 23: Wavy cylinder: Initial and three deformed configurations

5.5 Sphere in sphere

This example has been discussed in a similar three-dimensional setup in Puso and Laursen (2004a), and for the two-dimensional case in Fischer and Wriggers (2005). A solid sphere with radius $R = 0.6\,mm$, Young's modulus $E_S = 2000\,N/mm^2$ and Poisson's ratio $\nu_S = 0.3$ is placed within a less stiff hollow sphere with the material properties $E_H = 1000\,N/mm^2$ and $\nu_H = 0.0$. The inner radius of the hollow sphere is $R_i = 0.7\,mm$ and the outer radius is $R_a = 2.0\,mm$. A uniform vertical displacement is applied to all finite element nodes of the inner solid sphere up to a maximum displacement of $u_V = 1.125\,mm$, while the hollow sphere is fixed at the outside. The displacement boundary condition is applied in 20 time steps and the stabilization parameter is set to $\alpha_{\text{stab}} = 0.017$.

The initial as well as two deformed configurations of the solid sphere pressed into the hollow sphere are depicted in Fig. 24. It can be observed that the hollow sphere is highly distorted in the area of maximum contact pressure and that the inner solid sphere loses its circular shape. The developed contact domain method is able to

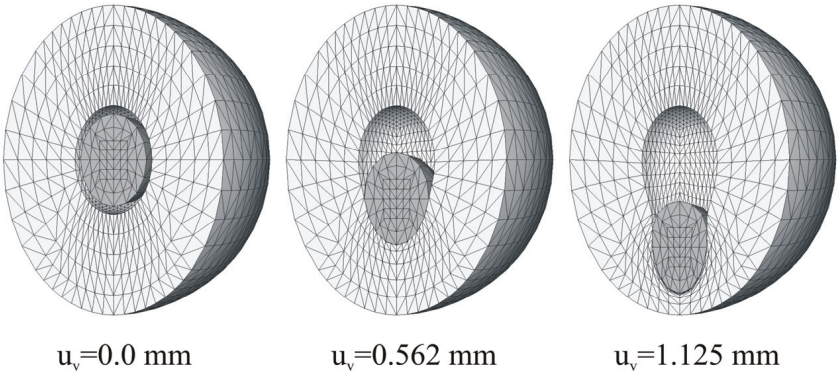

Figure 24: Initial and deformed configurations of solid sphere pressed into hollow sphere

capture the present finite deformations and the large changes of size and position of the contact area. Furthermore, the results compare quite well with those reported in [Fischer and Wriggers (2005)] and [Puso and Laursen (2004a)], where mortar segment-to-segment contact methods have been used. Finally, Puso and Laursen (2004a) have stated that the usage of a classical node-to-segment method failed in this example at a very early state, where only little deformation has occurred. Thus, this example underlines once again that the contact domain method developed herein has a higher robustness than classical node-to-segment methods.

5.6 Ball hits sheet

The last example was chosen to demonstrate the possibility to capture complex, dynamic contact scenarios including regions with self-contact. In Fig. 25 the geometric setup, the material properties as well as the finite element discretization is shown. An elastic ball, whose centre is initially located at a distance of $100.0\,mm$ from the obstacle, is thrown towards a flexible thin sheet with an initial velocity $v = 15.0\,mm/ms$. When the ball hits the sheet, it deforms significantly, such that it will get into contact with its own parts. The dynamic analysis is performed using a Generalized-α time integration [Chung and Hulbert (1993)] with a constant time step size of $\Delta t = 0.1\,ms$ and the stabilization parameter is set to $\alpha_{\text{stab}} = 0.03$.

In Fig. 26 and Fig. 27 the motion of the problem is shown at different time steps, without and with displaying the constructed contact domain patches, respectively. The presented contact algorithm performs quite well in this rather complex dynamic contact problem and can deal with the occurring self-contact scenario without any additional difficulty by construction.

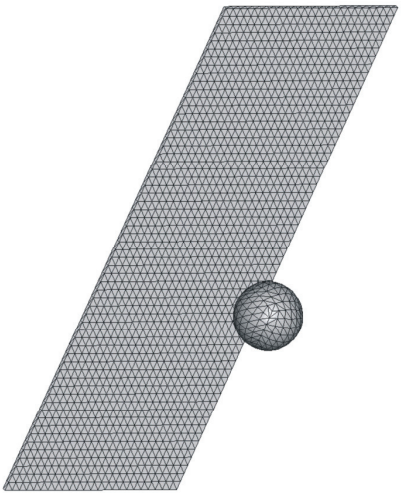

Figure 25: Ball-Sheet: Initial configuration and finite element discretization

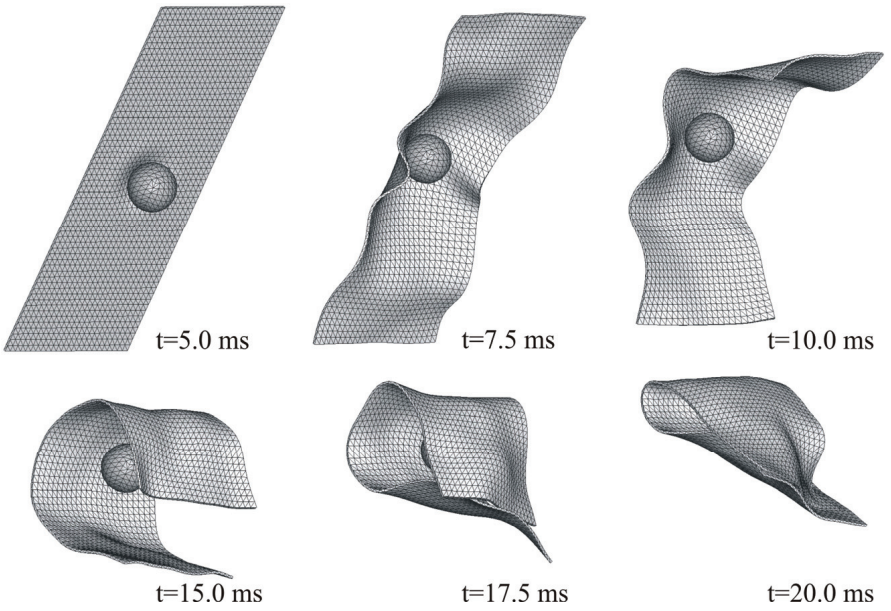

Figure 26: Ball-Sheet: Deformed configurations at different time steps – without plotting the contact domain patches

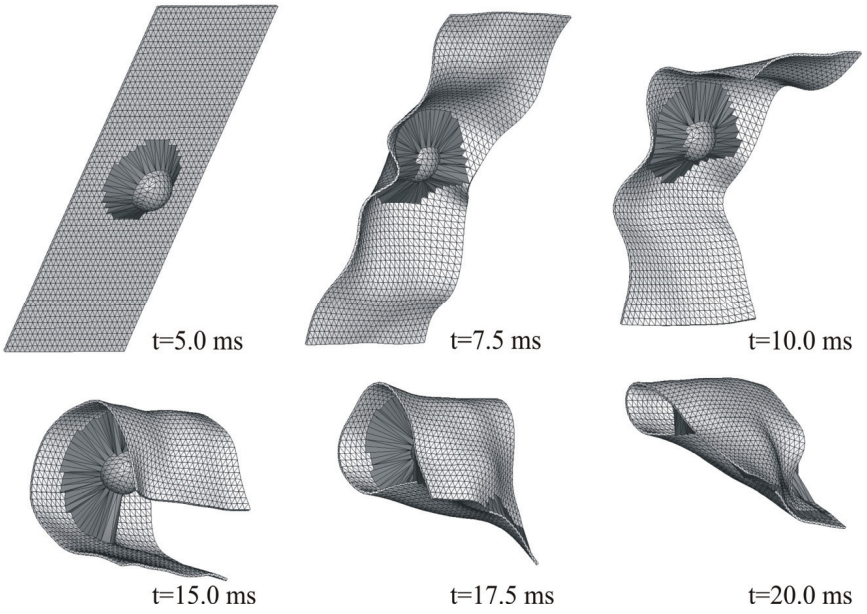

Figure 27: Ball-Sheet: Deformed configurations at different time steps – with plotting the contact domain patches

6 Concluding remarks

In this work, the generalization of the recently developed contact domain method [Oliver, Hartmann, Cante, Weyler and Hernández (2009); Hartmann, Oliver, Weyler, Cante and Hernández (2009)] to three-dimensional, frictionless, finite deformation, static and dynamic (self) contact problems has been presented. Some specific features of this contact domain method can be summarized as follows:

- The contact virtual work and the contact constraint equation are formulated on basis of a three-dimensional domain, called *contact domain*. This domain represents a unique pairing between potential contact boundaries and is generated via a constrained Delaunay tessellation.

- The contact domain is endowed with an additional displacement field interpolated from the incremental displacements of the contacting boundaries, which allows the definition of a dimensionless, strain-like quantity (the normal gap intensity) to formulate the geometrical contact constraint.

- The contact constraint enforcement is based on a generalization of the sta-

bilized Lagrange multiplier formulation, presented by Heintz and Hansbo (2006) for small deformation contact problems. Starting from a classical Lagrange multiplier formulation, the variational constraint equation is enhanced with a consistent stabilization term, which, due to the patch-wise constant approximation of the Lagrange multiplier, can be locally decoupled. This allows the condensation of the discrete Lagrange multipliers locally, on a patch level which eases the implementation of the contact algorithm.

Compared to other existing contact algorithms, the present formulation produces a solution, which does not depend on the choice of *slave* and *master* sides, as the contact pairing is defined through the contact domain. Thus, no projections of slave nodes/segments onto master segments have to be performed, circumventing the problem of possible pathological cases. As the Lagrange multipliers are introduced on the newly defined contact domain, the sometimes quite cumbersome numerical procedure of evaluating integrals of products of shape functions living on different surface grids, involved in the mortar method, is omitted. The employed contact pairing strategy constitutes a general approach in the context of contact searching algorithms, which does not necessitate any modifications in the treatment of self-contact.

The introduced stabilization term in the variational constraint equation leads to a non-symmetric contact stiffness matrix, which could be symmetrized by adding an appropriate stabilization term in the mechanical virtual work expression as well [Heintz and Hansbo (2006)]. This might have some benefits in the numerical implementation that need to be exploited in subsequent works. Typical for Nitsche type methods, the computation of the contact contributions depend on the stress field in the contacting bodies. Consequently, the resulting contact stiffness contributes as well to degrees of freedom of the finite elements at the contact boundary, which slightly increases the bandwidth of the final matrices. Furthermore, the linearization of the stresses at the boundaries of the contacting bodies depends upon the constitutive law and the type of finite element used therein. That means that the implementation of the proposed contact strategy cannot be as general as the one based on classical (non stabilized) Lagrange multiplier or penalty methods.

Approximating the three-dimensional contact domain with a full set of non-overlapping linear tetrahedral patches necessitates distinguishing between two types of contact patches. The so-called Type-A patch, sharing three vertex nodes with one boundary element and the so-called Type-B patch, having two vertex nodes placed on either side of the potential contact boundaries. While the Type-A contact patch shares many similarities with a classical node-to-segment contact element using a three-node master segment [Wriggers (2006)], the Type-B contact patch represents a new kind of three-dimensional contact element, whose consideration is the key to

allow this contact strategy exactly passing the contact patch test (see section 5.1).

A set of numerical examples presented in section 5 have demonstrated that the developed *contact domain method* produces reliable and accurate results. As already mentioned before, this strategy exactly passes the contact patch test (see section 5.1), independently of the value of the chosen stabilization parameter α_{stab}. The analysis of a Hertzian contact problem (see section 5.2) has shown that the described method provides accurate results. Furthermore, challenging problems, so far only captured by recently developed mortar based contact methods, as well as a highly dynamic problem involving self-contact, can be analyzed without any further modification of the algorithm. The consistent linearization of the normal contact contributions, given in section 3.5, guarantees a quadratic convergence within the Newton iteration, once the active contact set has converged. From the experience in various numerical examples, the authors can recommend a stabilization parameter $\alpha_{\text{stab}} \in [0.01 - 0.1]$ to produce reliable results for most applications.

Although the three-dimensional version of the contact domain method necessitates some more effort in the implementation compared to its two-dimensional counterpart [Oliver, Hartmann, Cante, Weyler and Hernández (2009); Hartmann, Oliver, Weyler, Cante and Hernández (2009)], like for example the consideration of two different kinds of contact patches, it is still relatively easy to code, due to the following reasons:

1. The element-wise constant approximation of the introduced Lagrange multipliers, together with the chosen discretization of the contacting bodies, allows a local elimination of the discrete Lagrange multipliers on patch level.

2. All the necessary integrations can be done analytically, circumventing possible difficulties in performing demanding numerical quadratures.

Furthermore, the evaluation of the contact forces and the contact stiffness contributions can be carried out locally for every individual contact domain patch, which only necessitates the information about the stress field in an adjacent "body" element.

As the performance of the presented contact strategy seems to be superior to classical node-to-segment formulations and comparable to recently developed mortar based contact algorithms, the *contact domain method* constitutes a sound alternative in the field of computational contact mechanics. However, further investigations, like incorporating friction to the three-dimensional setting, which will be the scope of future work, are necessary.

Acknowledgement: The first author gratefully acknowledges the support of the German Research Foundation through the grant HA 5433/1-1. Furthermore, the financial support from the Spanish Ministry of Science and Innovation, through grant BIA2008-00411 and from the Catalan government, through grant 2009 SGR 1510, is gratefully acknowledged.

References

Bardenhagen, S.G.; Guilkey, J.E.; Roessig, K.M.; Brackbill, J.U.; Witzel, W.M; Foster, J.C. (2001): An Improved Contact Algorithm for the Material Point Method and Application to Stress Propagation in Granular Material. *CMES: Computer Modeling in Engineering & Sciences*, vol. 2, no. 4, pp. 509–522.

Belgacem, F.; Hild, P.; Laborde, P. (1998): The mortar finite element method for contact problems. *Mathematical and Computer Modeling*, vol. 28, pp. 263–271.

Bernardi, C.; Debit, N.; Maday, Y. (1990): Coupling Finite Elements and Spectral Methods: First Results. *Mathematics of Computation*, vol. 54, pp. 21–39.

Bernardi, C.; Maday, Y.; Patera, A. (1993): Domain decomposition by the mortar element method, in *Asymptotic and Numerical Methods for Partial Differential Equations with Critical Parameters*, H. Kasper and M. Garby, Eds. Dordrecht, Netherlands: Kluver Academic Publisher, pp. 269–286.

Bernardi, C.; Maday, Y.; Patera, A. (1994): A new nonconforming approach to domain decomposition: the mortar element method, in *Nonlinear partial differential equations and their applications – Collège de France Seminar*, vol. XI, H. Brezis and J. Lions, Eds.: Longman, Harlow , pp. 13–51.

Bonet, J.; Wood, R.D. (1997): *Nonlinear continuum mechanics for finite element analysis*. Cambridge, UK: Cambridge University Press.

Chung, J.; Hulbert, G.M. (1993): A Time Integration Algorithm for Structural Dynamics With Improved Numerical Dissipation: The Generalized-alpha method, *Journal of Applied Mechanics*, vol. 60, pp. 371–375.

Fischer, K.A.; Wriggers, P. (2005): Frictionless 2D Contact formulations for finite deformations based on the mortar method, *Computational Mechanics*, vol. 36, pp. 226–244.

Fischer, K.A.; Wriggers, P. (2006): Mortar based frictional contact formulation for higher order interpolations using the moving friction cone, *Computer Methods in Applied Mechanics and Engineering*, vol. 195, pp. 5020–5036.

Hallquist, J.; Goudreau, G.; Benson, D. (1985): Sliding interfaces with contact-impact in large-scale Lagrangian computations, *Computer Methods in Applied Mechanics and Engineering*, vol. 51, pp. 107–137.

Hartmann, S. (2007): *Kontaktanalyse dünnwandiger Strukturen bei großen Deformationen*, Ph.D. Thesis, Report No 49, Institut für Baustatik, Universtiät Stuttgart, Germany.

Hartmann, S.; Brunssen, S.; Ramm, E.; Wohlmuth, B. (2007): Unilateral nonlinear dynamic contact of thin-walled structures using a primal-dual active set strategy, *International Journal for Numerical Methods in Engineering*, vol. 70, pp. 883–912.

Hartmann, S.; Oliver, J.; Weyler, R.; Cante, J.C.; Hernández, J. (2009): A contact domain method for large deformation frictional contact problems. Part 2: Numerical aspects, *Computer Methods in Applied Mechanics and Engineering*, vol. 198, pp. 2607–2631.

Hartmann, S.; Ramm, E. (2008): A mortar based contact formulation for nonlinear dynamics using dual Lagrange multipliers, *Finite Elements in Analysis and Design*, vol. 44, pp. 245–258.

Heege, A.; Alart, P. (1996): A frictional contact element for strongly curved contact problems, *International Journal for Numerical Methods in Engineering*, vol. 39, pp. 165–184.

Heintz, P.; Hansbo, P. (2006): Stabilized Lagrange multiplier method for bilateral elastic contact with friction, *Computer Methods in Applied Mechanics and Engineering*, vol. 195, pp. 4323–4333.

Hüeber, S.; Stadler, G.; Wohlmuth, B.I. (2008): A primal-dual active set algorithm for three-dimensional contact problems with coulomb friction, *SIAM Journal on Scientific Computing*, vol. 30, pp. 572–596.

Hüeber, S.; Wohlmuth, B. (2005): A primal-dual active set strategy for non-linear multibody contact problems, *Computer Methods in Applied Mechanics and Engineering*, vol. 194, pp. 3147–3166.

Idelsohn, S.R.; Onate, E.; Calvo, N.; Del Pin, F. (2003): The meshless finite element method, *International Journal for Numerical Methods in Engineering*, vol. 58, pp. 893–912.

Kikuchi, N.; Oden, J.T. (1988): *Contact Problems in Elasticity: A Study of Variational Inequalities and Finite Element Methods*. SIAM: Philadelphia.

Laursen, T.A. (2002): *Computational Contact and Impact Mechanics*. Springer.

Mc Devitt, T.M.; Laursen, T.A. (2000): A mortar-finite element formulation for frictional contact problems, *International Journal for Numerical Methods in Engineering*, vol. 48, pp. 1525–1547.

Nitsche, J. (1971): Über ein Variationsprinzip zur Lösung von Dirichlet-Problemen bei Verwendung von Teilräumen, die keinen Randbedingungen unterworfen sind,

Abhandlungen in der Mathematik an der Universität Hamburg, vol. 36, pp. 9–15.

Oliver, J.; Hartmann, S.; Cante, J.C.; Weyler, R.; Hernández, J. (2009): A contact domain method for large deformation frictional contact problems. Part 1: Theoretical basis, *Computer Methods in Applied Mechanics and Engineering*, vol. 198, pp. 2591–2606.

Papadopoulos, P.; Taylor, R. (1992): A mixed formulation for the finite element solution of contact problems, *Computer Methods in Applied Mechanics and Engineering*, vol. 94, pp. 373–389.

Pietrzak, G.; Curnier, A. (1999): Large deformation frictional contact mechanics: continuum formulation and augmented Lagrangian treatment, *Computer Methods in Applied Mechanics and Engineering*, vol. 177, pp. 351–381.

Popp, A.; Gee, M.W.; Wall, W.A. (2009): A finite deformation mortar contact formulation using a primal-dual active set strategy, *International Journal for Numerical Methods in Engineering*, vol. 79, pp. 1354–1391.

Puso, M.; Laursen, T. (2002): A 3d contact smoothing method using gregory patches, *International Journal for Numerical Methods in Engineering*, vol. 54, pp. 1161–1194.

Puso, M.; Laursen, T. (2004a): A mortar segment-to-segment contact method for large deformation solid mechanics, *Computer Methods in Applied Mechanics and Engineering*, vol. 193, pp. 601–629.

Puso, M.; Laursen, T. (2004b): A mortar segment-to-segment frictional contact method for large deformations, *Computer Methods in Applied Mechanics and Engineering*, vol. 193, pp. 4891–4913.

Puso, M.A.; Laursen, T.A.; Solberg, J. (2008): A segment-to-segment mortar contact method for quadratic elements and large deformations, *Computer Methods in Applied Mechanics and Engineering*, vol. 197, pp. 555–566.

Simo, J.; Wriggers, P.; Taylor, R. (1985): A perturbed Lagrangian formulation for the finite element solution of contact problems, *Computer Methods in Applied Mechanics and Engineering*, vol. 50, pp. 163–180.

Simo, J.C.; Laursen, T.A. (1992): An augmented Lagrangian treatment of contact problems involving friction, *Computers and Structures*, vol. 42, pp. 97–116.

Taylor, R.; Wriggers, P. (1999): Smooth surface discretization for large deformation frictionless contact, Technical Report UCB/SEM-99-04, University of California, Berkeley.

Vignjevic, R.; De Vuyst, T.; Campbell, J.C. (2006): A Frictionless Contact Algorithm for Meshless Methods. *CMES: Computer Modeling in Engineering & Sciences*, vol. 13, no. 1, pp. 35–47.

Willner, K. (2009): Constitutive Contact Laws in Structural Dynamics. *CMES: Computer Modeling in Engineering & Sciences*, vol. 48, no. 3, pp. 303–336.

Wriggers, P. (1995): Finite Element Algorithms for Contact Problems, *Archives of Computational Methods in Engineering*, vol. 2, pp. 1–49.

Wriggers, P. (2006): *Computational Contact Mechanics*, 2^{nd} ed. New York: Springer Berlin/Heidelberg.

Wriggers, P.; Krstulovic-Opara, L.; Korelc, J. (2001): Smooth c1-interpolations for two-dimensional frictional contact problems, *International Journal for Numerical Methods in Engineering*, vol. 51, pp. 1469–1495.

Wriggers, P.; Zavarise, G. (2008): A formulation for frictionless contact problems using a weak form introduced by Nitsche, *Computational Mechanics*, vol. 41, pp. 407–420.

Yang, B.; Laursen, T.A.; Meng, X. (2005): Two dimensional mortar contact methods for large deformation frictional sliding, *International Journal for Numerical Methods in Engineering*, vol. 62, pp. 1183–1225.

Zavarise, G.; Wriggers, P. (1998): A segment-to-segment contact strategy, *Mathematical and Computer Modelling*, vol. 28, pp. 497–515.

Zienkiewicz, O.C.; Taylor, R.L. (2000): *The Finite Element Method*, Oxford UK: Butterworth-Heinemann.

Appendix A Variations and linearizations

A.1 Variation an linearization of current unit normal vector

The patch-wise constant, unit normal vector in the current configuration is given with

$$\mathbf{n} = \frac{\mathbf{t}_1 \times \mathbf{t}_2}{\|\mathbf{t}_1 \times \mathbf{t}_2\|} = \frac{\mathbf{t}_1 \times \mathbf{t}_2}{\sqrt{(\mathbf{t}_1 \times \mathbf{t}_2) \cdot (\mathbf{t}_1 \times \mathbf{t}_2)}} \tag{97}$$

where $\mathbf{t}_\alpha$ are the current (not normalized) covariant tangent vectors. Then its variation is derived with

$$\delta \mathbf{n} = \frac{1}{(\|\mathbf{t}_1 \times \mathbf{t}_2\|)^2} \left\{ \|\mathbf{t}_1 \times \mathbf{t}_2\| \, \delta (\mathbf{t}_1 \times \mathbf{t}_2) - (\mathbf{t}_1 \times \mathbf{t}_2) \left[\frac{\mathbf{t}_1 \times \mathbf{t}_2}{\|\mathbf{t}_1 \times \mathbf{t}_2\|} \cdot \delta (\mathbf{t}_1 \times \mathbf{t}_2) \right] \right\} \tag{98}$$

Introducing the definition of the unit normal vector from Eq.97 leads to

$$\begin{aligned} \delta \mathbf{n} &= \frac{1}{\|\mathbf{t}_1 \times \mathbf{t}_2\|} \{ \delta (\mathbf{t}_1 \times \mathbf{t}_2) - \mathbf{n} [\mathbf{n} \cdot \delta (\mathbf{t}_1 \times \mathbf{t}_2)] \} \\ \rightarrow \delta \mathbf{n} &= \frac{1}{\|\mathbf{t}_1 \times \mathbf{t}_2\|} (1 - \mathbf{n} \otimes \mathbf{n}) \cdot \delta (\mathbf{t}_1 \times \mathbf{t}_2) \end{aligned} \tag{99}$$

Now using

$$\mathbf{1}-\mathbf{n}\otimes\mathbf{n}=t^{\alpha\beta}\mathbf{t}_\alpha\otimes\mathbf{t}_\beta \tag{100}$$

where $t^{\alpha\beta}$ is the contravariant metric tensor,

$$\delta\left(\mathbf{t}_1\times\mathbf{t}_2\right)=\delta\mathbf{t}_1\times\mathbf{t}_2+\mathbf{t}_1\times\delta\mathbf{t}_2 \tag{101}$$

and

$$\begin{aligned}\delta\mathbf{t}_\alpha&=\delta\left(\mathbf{f}\cdot\mathbf{T}_\alpha\right)=GRAD\left(\delta\mathbf{u}\right)\cdot\mathbf{T}_\alpha\\&=grad\left(\delta\mathbf{u}\right)\cdot\mathbf{f}\cdot\mathbf{T}_\alpha=grad\left(\delta\mathbf{u}\right)\cdot\mathbf{t}_\alpha=\frac{\partial\delta\mathbf{u}}{\partial t_\alpha}\end{aligned} \tag{102}$$

finally leads to

$$\delta\mathbf{n}=-t^{\alpha\beta}\left(\mathbf{t}_\alpha\otimes\mathbf{n}\right)\cdot\delta\mathbf{t}_\beta=-t^{\alpha\beta}\left(\mathbf{t}_\alpha\otimes\mathbf{n}\right)\cdot\frac{\partial\delta\mathbf{u}}{\partial t_\beta} \tag{103}$$

As the linearization takes the same form as the variation it can be written with:

$$\Delta\mathbf{n}=-t^{\alpha\beta}\left(\mathbf{t}_\alpha\otimes\mathbf{n}\right)\cdot\frac{\partial\Delta\mathbf{u}}{\partial t_\beta} \tag{104}$$

A.2 Variation of the normal gap intensity

From Eq.12 follows

$$\begin{aligned}&\bar{g}_N=sign\left(G_N\right)\mathbf{n}\cdot\mathbf{f}\cdot\mathbf{N}\\&\Rightarrow\delta\bar{g}_N=sign\left(G_N\right)\left(\delta\mathbf{n}\cdot\mathbf{f}\cdot\mathbf{N}+\mathbf{n}\cdot\delta\mathbf{f}\cdot\mathbf{N}\right)\end{aligned} \tag{105}$$

Then using Eq.103 and the unity

$$\mathbf{1}=\mathbf{n}\otimes\mathbf{n}+t^{\alpha\beta}\mathbf{t}_\alpha\otimes\mathbf{t}_\beta \tag{106}$$

leads to

$$\begin{aligned}\delta\bar{g}_N=sign\left(G_N\right)\Big(-t^{\alpha\beta}\left(\mathbf{n}\cdot grad\left(\delta\mathbf{u}\right)\cdot\mathbf{t}_\beta\right)\mathbf{t}_\alpha\cdot\mathbf{f}\cdot\mathbf{N}+\left(\mathbf{n}\cdot grad\left(\delta\mathbf{u}\right)\cdot\mathbf{n}\right)\mathbf{n}\cdot\mathbf{f}\cdot\mathbf{N}\\+t^{\alpha\beta}\left(\mathbf{n}\cdot grad\left(\delta\mathbf{u}\right)\cdot\mathbf{t}_\alpha\right)\mathbf{t}_\beta\cdot\mathbf{f}\cdot\mathbf{N}\Big)\end{aligned} \tag{107}$$

So the variation of the normal gap intensity then read:

$$\delta\bar{g}_N=\bar{g}_N\mathbf{n}\cdot grad\left(\delta\mathbf{u}\right)\cdot\mathbf{n} \tag{108}$$

A.3 Linearization of the variation of the normal gap intensity

Starting from Eq.108, the linearization reads

$$\Delta\delta\bar{g}_N = \Delta\bar{g}_N\mathbf{n}\cdot\frac{\partial\delta\mathbf{u}}{\partial n} + \bar{g}_N\Delta\mathbf{n}\cdot\frac{\partial\delta\mathbf{u}}{\partial n} + \bar{g}_N\mathbf{n}\cdot\Delta\left(\frac{\partial\delta\mathbf{u}}{\partial n}\right) \tag{109}$$

where the linearization of the normal gap intensity has the same structure as Eq.108

$$\Delta\bar{g}_N = \bar{g}_N\mathbf{n}\cdot grad\,(\Delta\mathbf{u})\cdot\mathbf{n} \tag{110}$$

and the linearization of the current normal vector is given in Eq.104. The linearization of the n-directional derivative reads

$$\Delta\left(\frac{\partial\delta\mathbf{u}}{\partial n}\right) = \Delta\left(grad\,(\delta\mathbf{u})\cdot\mathbf{n}\right) = \Delta\left(grad\,(\delta\mathbf{u})\right)\cdot\mathbf{n} + grad\,(\delta\mathbf{u})\cdot\Delta\mathbf{n} \tag{111}$$

with

$$\begin{aligned}\Delta\left(grad\,(\delta\mathbf{u})\right) &= \Delta\left(GRAD\,(\delta\mathbf{u})\cdot\mathbf{f}^{-1}\right) = \underbrace{GRAD\,(\delta\mathbf{u})}_{grad(\delta\mathbf{u})\cdot\mathbf{f}}\cdot\underbrace{\Delta\mathbf{f}^{-1}}_{-\mathbf{f}^{-1}\cdot grad(\Delta\mathbf{u})} \\ \Rightarrow \Delta\left(grad\,(\delta\mathbf{u})\right) &= -grad\,(\delta\mathbf{u})\cdot grad\,(\Delta\mathbf{u})\end{aligned} \tag{112}$$

Inserting Eq.104 and Eq.112 into Eq.111 leads after some standard algebraic transformations to

$$\Delta\left(\frac{\partial\delta\mathbf{u}}{\partial n}\right) = -\left(\frac{\partial\delta\mathbf{u}}{\partial n}\right)\left(\mathbf{n}\cdot\frac{\partial\Delta\mathbf{u}}{\partial n}\right) - t^{\alpha\beta}\left(\frac{\partial\delta\mathbf{u}}{\partial t_\alpha}\right)\left(t_\beta\cdot\frac{\partial\Delta\mathbf{u}}{\partial n} + \mathbf{n}\cdot\frac{\partial\Delta\mathbf{u}}{\partial t_\beta}\right) \tag{113}$$

Using this expression, the linearization of the variation of the normal gap intensity finally (Eq.109) reads

$$\begin{aligned}\Delta\delta\bar{g}_N = -\bar{g}_N\Bigg[&t^{\alpha\beta}\left(\mathbf{n}\cdot\frac{\partial\delta\mathbf{u}}{\partial t_\alpha}\right)\left(\mathbf{n}\cdot\frac{\partial\Delta\mathbf{u}}{\partial t_\beta}\right) + t^{\alpha\beta}\left(\mathbf{n}\cdot\frac{\partial\delta\mathbf{u}}{\partial t_\alpha}\right)\left(\mathbf{t}_\beta\cdot\frac{\partial\Delta\mathbf{u}}{\partial n}\right) \\ &+ t^{\alpha\beta}\left(\mathbf{t}_\alpha\cdot\frac{\partial\delta\mathbf{u}}{\partial n}\right)\left(\mathbf{n}\cdot\frac{\partial\Delta\mathbf{u}}{\partial t_\beta}\right)\Bigg]\end{aligned} \tag{114}$$

Appendix B Linearization of first Piola-Kirchhoff stresses

The first Piola-Kirchhoff stress tensor $\mathbf{P}$ can be written in terms of the material deformation gradient $\mathbf{F}$ and the second Piola-Kirchhoff stress tensor $\mathbf{S}$ ([Bonet and Wood (1997)])

$$\mathbf{P} = \mathbf{F}\cdot\mathbf{S}. \tag{115}$$

Its linearization yields

$$\Delta \mathbf{P} = \Delta \mathbf{F} \cdot \mathbf{S} + \mathbf{F} \cdot \Delta \mathbf{S}, \tag{116}$$

with the linearization of the second Piola-Kirchhoff stress tensor

$$\Delta \mathbf{S} = \mathbf{C}^{\text{tang}} : \Delta \mathbf{E}, \tag{117}$$

where $\mathbf{C}^{\text{tang}}$ is the 4^{th} order constitutive tangent operator, which relates the incremental second Piola-Kirchhoff stresses $\Delta\mathbf{S}$ with the incremental non-linear Green-Lagrange strains $\Delta\mathbf{E}$.

B.1 Matrix notation

Using a three dimensional, 4-noded finite element formulation for the discretization of the "body" elements, the linearization of the first Piola-Kirchhoff stress tensor can be written in matrix formulation. With the definition of the vector $\Delta^{II}\mathbf{d}_p^T$ of incremental nodal displacements in Eq.75, based on the node numbering given for Type-A (see Fig. 6) and Type-B patches (see Fig. 9), respectively, the following vectors and matrices are defined:

The linearization of the material deformation gradient

$$\Delta \bar{\mathbf{F}}_{(9\times 1)} = \begin{pmatrix} \Delta F_{11} \\ \Delta F_{22} \\ \Delta F_{33} \\ \Delta F_{12} \\ \Delta F_{21} \\ \Delta F_{23} \\ \Delta F_{32} \\ \Delta F_{13} \\ \Delta F_{31} \end{pmatrix} = \tilde{\mathbf{B}}_{(9\times 12)} \Delta \mathbf{d}_{(12\times 1)} \tag{118}$$

with the linear B-operator matrix

$$\tilde{\mathbf{B}}_{(9\times12)} = \begin{pmatrix} N_{1,1} & 0 & 0 & N_{2,1} & 0 & 0 & N_{3,1} & 0 & 0 & N_{4,1} & 0 & 0 \\ 0 & N_{1,2} & 0 & 0 & N_{2,2} & 0 & 0 & N_{3,2} & 0 & 0 & N_{4,2} & 0 \\ 0 & 0 & N_{1,3} & 0 & 0 & N_{2,3} & 0 & 0 & N_{3,3} & 0 & 0 & N_{4,3} \\ N_{1,2} & 0 & 0 & N_{2,2} & 0 & 0 & N_{3,2} & 0 & 0 & N_{4,2} & 0 & 0 \\ 0 & N_{1,1} & 0 & 0 & N_{2,1} & 0 & 0 & N_{3,1} & 0 & 0 & N_{4,1} & 0 \\ 0 & N_{1,3} & 0 & 0 & N_{2,3} & 0 & 0 & N_{3,3} & 0 & 0 & N_{4,3} & 0 \\ 0 & 0 & N_{1,2} & 0 & 0 & N_{2,2} & 0 & 0 & N_{3,2} & 0 & 0 & N_{4,2} \\ N_{1,3} & 0 & 0 & N_{2,3} & 0 & 0 & N_{3,3} & 0 & 0 & N_{4,3} & 0 & 0 \\ 0 & 0 & N_{1,1} & 0 & 0 & N_{2,1} & 0 & 0 & N_{3,1} & 0 & 0 & N_{4,1} \end{pmatrix}, \tag{119}$$

where $N_{I,J}$ are the derivatives of the shape functions N_I in the adjacent "body" element, with respect to the coordinates of the previous configuration.

The linearization of the second Piola-Kirchhoff stress tensor

$$\begin{aligned} \Delta\bar{\mathbf{S}}_{(9\times1)} &= \begin{pmatrix} \Delta S_{11} \\ \Delta S_{22} \\ \Delta S_{33} \\ \Delta S_{12} \\ \Delta S_{21} \\ \Delta S_{23} \\ \Delta S_{32} \\ \Delta S_{13} \\ \Delta S_{31} \end{pmatrix} = \mathbf{D}_{(9\times9)}\Delta\bar{\mathbf{E}}_{(9\times1)} = \mathbf{D}_{(9\times9)} \begin{pmatrix} \Delta E_{11} \\ \Delta E_{22} \\ \Delta E_{33} \\ \Delta E_{12} \\ \Delta E_{21} \\ \Delta E_{23} \\ \Delta E_{32} \\ \Delta E_{13} \\ \Delta E_{31} \end{pmatrix} \\ &= \mathbf{D}_{(9\times9)}\mathbf{B}_{(9\times12)}\Delta\mathbf{d}_{(12\times1)} \end{aligned} \tag{120}$$

with the incremental constitutive tangent matrix

$$\mathbf{D}_{(9\times 9)} = \begin{pmatrix} C^{tang}_{1111} & C^{tang}_{1122} & C^{tang}_{1133} & C^{tang}_{1112} & C^{tang}_{1121} & C^{tang}_{1123} & C^{tang}_{1132} & C^{tang}_{1113} & C^{tang}_{1131} \\ C^{tang}_{2211} & C^{tang}_{2222} & C^{tang}_{2233} & C^{tang}_{2212} & C^{tang}_{2221} & C^{tang}_{2223} & C^{tang}_{2232} & C^{tang}_{2213} & C^{tang}_{2231} \\ C^{tang}_{3311} & C^{tang}_{3322} & C^{tang}_{3333} & C^{tang}_{3312} & C^{tang}_{3321} & C^{tang}_{3323} & C^{tang}_{3332} & C^{tang}_{3313} & C^{tang}_{3331} \\ C^{tang}_{1211} & C^{tang}_{1222} & C^{tang}_{1233} & C^{tang}_{1212} & C^{tang}_{1221} & C^{tang}_{1223} & C^{tang}_{1232} & C^{tang}_{1213} & C^{tang}_{1231} \\ C^{tang}_{2111} & C^{tang}_{2122} & C^{tang}_{2133} & C^{tang}_{2112} & C^{tang}_{2121} & C^{tang}_{2123} & C^{tang}_{2132} & C^{tang}_{2113} & C^{tang}_{2131} \\ C^{tang}_{2311} & C^{tang}_{2322} & C^{tang}_{2333} & C^{tang}_{2312} & C^{tang}_{2321} & C^{tang}_{2323} & C^{tang}_{2332} & C^{tang}_{2313} & C^{tang}_{2331} \\ C^{tang}_{3211} & C^{tang}_{3222} & C^{tang}_{3233} & C^{tang}_{3212} & C^{tang}_{3221} & C^{tang}_{3223} & C^{tang}_{3232} & C^{tang}_{3213} & C^{tang}_{3231} \\ C^{tang}_{1311} & C^{tang}_{1322} & C^{tang}_{1333} & C^{tang}_{1312} & C^{tang}_{1321} & C^{tang}_{1323} & C^{tang}_{1332} & C^{tang}_{1313} & C^{tang}_{1331} \\ C^{tang}_{3111} & C^{tang}_{3122} & C^{tang}_{3133} & C^{tang}_{3112} & C^{tang}_{3121} & C^{tang}_{3123} & C^{tang}_{3132} & C^{tang}_{3113} & C^{tang}_{3131} \end{pmatrix} \tag{121}$$

and the non-linear B-operator matrix

$$\mathbf{B}_{(9\times 12)} = \begin{pmatrix} \mathbf{B}_1 & \mathbf{B}_2 & \mathbf{B}_3 & \mathbf{B}_4 \end{pmatrix} \tag{122}$$

with

$$\mathbf{B}_I = \begin{pmatrix} F_{11}N_{I,1} & F_{21}N_{I,1} & F_{31}N_{I,1} \\ F_{12}N_{I,2} & F_{22}N_{I,2} & F_{32}N_{I,2} \\ F_{13}N_{I,3} & F_{23}N_{I,3} & F_{33}N_{I,3} \\ \frac{1}{2}\left(F_{11}N_{I,2}+F_{12}N_{I,1}\right) & \frac{1}{2}\left(F_{21}N_{I,2}+F_{22}N_{I,1}\right) & \frac{1}{2}\left(F_{31}N_{I,2}+F_{32}N_{I,1}\right) \\ \frac{1}{2}\left(F_{11}N_{I,2}+F_{12}N_{I,1}\right) & \frac{1}{2}\left(F_{21}N_{I,2}+F_{22}N_{I,1}\right) & \frac{1}{2}\left(F_{31}N_{I,2}+F_{32}N_{I,1}\right) \\ \frac{1}{2}\left(F_{12}N_{I,3}+F_{13}N_{I,2}\right) & \frac{1}{2}\left(F_{22}N_{I,3}+F_{23}N_{I,2}\right) & \frac{1}{2}\left(F_{32}N_{I,3}+F_{33}N_{I,2}\right) \\ \frac{1}{2}\left(F_{12}N_{I,3}+F_{13}N_{I,2}\right) & \frac{1}{2}\left(F_{22}N_{I,3}+F_{23}N_{I,2}\right) & \frac{1}{2}\left(F_{32}N_{I,3}+F_{33}N_{I,2}\right) \\ \frac{1}{2}\left(F_{13}N_{I,1}+F_{11}N_{I,3}\right) & \frac{1}{2}\left(F_{23}N_{I,1}+F_{21}N_{I,3}\right) & \frac{1}{2}\left(F_{33}N_{I,1}+F_{31}N_{I,3}\right) \\ \frac{1}{2}\left(F_{13}N_{I,1}+F_{11}N_{I,3}\right) & \frac{1}{2}\left(F_{23}N_{I,1}+F_{21}N_{I,3}\right) & \frac{1}{2}\left(F_{33}N_{I,1}+F_{31}N_{I,3}\right) \end{pmatrix}. \tag{123}$$

Furthermore, the values of the material deformation gradient and the second Piola-Kirchhoff stress tensor are organized in matrices:

$$\bar{\mathbf{F}}_{(9\times 9)} = \begin{pmatrix} F_{11} & 0 & 0 & 0 & F_{12} & 0 & 0 & 0 & F_{13} \\ 0 & F_{22} & 0 & F_{21} & 0 & 0 & F_{23} & 0 & 0 \\ 0 & 0 & F_{33} & 0 & 0 & F_{32} & 0 & F_{31} & 0 \\ 0 & F_{12} & 0 & F_{11} & 0 & 0 & F_{13} & 0 & 0 \\ F_{21} & 0 & 0 & 0 & F_{22} & 0 & 0 & 0 & F_{23} \\ 0 & 0 & F_{23} & 0 & 0 & F_{22} & 0 & F_{21} & 0 \\ 0 & F_{32} & 0 & F_{31} & 0 & 0 & F_{33} & 0 & 0 \\ 0 & 0 & F_{13} & 0 & 0 & F_{12} & 0 & F_{11} & 0 \\ F_{31} & 0 & 0 & 0 & F_{32} & 0 & 0 & 0 & F_{33} \end{pmatrix}$$

and

$$\bar{\mathbf{S}}_{(9\times 9)} = \begin{pmatrix} S_{11} & 0 & 0 & S_{21} & 0 & 0 & 0 & S_{31} & 0 \\ 0 & S_{22} & 0 & 0 & S_{12} & S_{32} & 0 & 0 & 0 \\ 0 & 0 & S_{33} & 0 & 0 & 0 & S_{23} & 0 & S_{13} \\ S_{12} & 0 & 0 & S_{22} & 0 & 0 & 0 & S_{32} & 0 \\ 0 & S_{21} & 0 & 0 & S_{11} & S_{31} & 0 & 0 & 0 \\ 0 & S_{23} & 0 & 0 & S_{13} & S_{33} & 0 & 0 & 0 \\ 0 & 0 & S_{32} & 0 & 0 & 0 & S_{22} & 0 & S_{12} \\ S_{13} & 0 & 0 & S_{23} & 0 & 0 & 0 & S_{33} & 0 \\ 0 & 0 & S_{31} & 0 & 0 & 0 & S_{21} & 0 & S_{11} \end{pmatrix} \tag{124}$$

Thus the linearization of the first Piola-Kirchhoff stress tensor is given in matrix form:

$$\Delta\bar{\mathbf{P}}_{(9\times 1)} = \begin{pmatrix} \Delta P_{11} \\ \Delta P_{22} \\ \Delta P_{33} \\ \Delta P_{12} \\ \Delta P_{21} \\ \Delta P_{23} \\ \Delta P_{32} \\ \Delta P_{13} \\ \Delta P_{31} \end{pmatrix} = \left(\bar{\mathbf{S}}_{(9\times 9)}\tilde{\mathbf{B}}_{(9\times 12)} + \bar{\mathbf{F}}_{(9\times 9)}\mathbf{D}_{(9\times 9)}\mathbf{B}_{(9\times 12)}\right)\Delta^{II}\mathbf{d}_{(12\times 1)} \tag{125}$$